Monthly Notices of the ROYAL ASTRONOMICAL SOCIETY

MNRAS **514,** 1088–1106 (2022) https://doi.org/10.1093/mnras/stac1461
Advance Access publication 2022 May 30

Modelling the secular evolution of protoplanetary disc dust sizes – a comparison between the viscous and magnetic wind case

Francesco Zagaria [1]★ Giovanni P. Rosotti [2,3] Cathie J. Clarke[1] and Benoît Tabone [4]

[1]*Institute of Astronomy, University of Cambridge, Madingley Road, Cambridge CB3 0HA, UK*
[2]*School of Physics and Astronomy, University of Leicester, Leicester LE1 7RH, UK*
[3]*Leiden Observatory, Leiden University, PO Box 9513, NL-2300 RA Leiden, the Netherlands*
[4]*Institut d'Astrophysique Spatiale, Université Paris-Saclay, CNRS, F-91405 Orsay, France*

Accepted 2022 May 17. Received 2022 April 26; in original form 2022 March 8

ABSTRACT

For many years, protoplanetary discs have been thought to evolve viscously: angular momentum redistribution leads to accretion and outward disc spreading. Recently, the hypothesis that accretion is due, instead, to angular momentum removal by magnetic winds gained new popularity: no disc spreading is expected in this case. In this paper, we run several 1D gas and dust simulations to make predictions on the time evolution of disc sizes *in the dust* and to assess whether they can be used to understand how discs evolve. We show that viscous and magnetic wind models have very different dust disc radii. In particular, magnetohydrodynamic wind models are compact and their sizes either remain constant or decrease with time. On the contrary, discs become larger with time in the viscous case (when $\alpha \gtrsim 10^{-3}$). Although current observations lack enough sensitivity to discriminate between these two scenarios, higher sensitivity surveys could be fruitful to this goal on a 1–10 Myr age range. When compared with the available ALMA (Atacama Large Millimeter/submillimeter Array) Band 7 data, both viscous and magnetic wind models are compatible with the observationally inferred dust radii in Lupus, Chamaeleon I, and Upper Sco. Furthermore, in the drift-dominated regime, the size–luminosity correlation is reproduced in Lupus, both in Band 7 and 3, while in Upper Sco a different slope than in the data is predicted. Sub-structures (potentially undetected) can explain several outliers with large observed sizes. Higher angular-resolution observations will be helpful to test our predictions in the case of more compact discs, expected in both frameworks, particularly at the age of Upper Sco.

Key words: accretion, accretion discs – MHD – methods: numerical – planets and satellites: formation – protoplanetary discs – submillimetre: planetary systems.

1 INTRODUCTION

Planets form in discs of gas and dust orbiting young stars. Knowledge of the evolutionary processes that such planet-forming discs undergo before dissipating is essential to any planet-formation theory (e.g. Morbidelli & Raymond 2016) and key to understanding the properties of the currently observed exoplanets, such as their system architectures (Winn & Fabrycky 2015), their composition (Madhusudhan 2019), and ultimately their potential to host life (e.g. by the presence of water and organics; Öberg & Bergin 2021).

Disc evolution is a long-standing problem motivated by the evidence that most new-born stars accrete gas (Hartmann, Herczeg & Calvet 2016). Since the pioneering work of Shakura & Sunyaev (1973) and Lynden-Bell & Pringle (1974), protoplanetary discs have been thought to evolve under the effect of viscosity (an averaged effective turbulence). In this picture, viscosity allows for accretion on to the forming star transporting some material outwards, in a process known as *viscous spreading*. Nevertheless, the physical origin and magnitude of viscosity are still debated (e.g. Turner et al. 2014). For this reason, Shakura & Sunyaev (1973) introduced a parametrization of viscosity in terms of a coefficient, $\alpha_{\rm SS}$, embodying our ignorance of the physical mechanisms behind turbulence. Traditionally, the magnetorotational instability (MRI) has been invoked as a possible source of turbulence in the inner disc (Balbus & Hawley 1991), while gravitational instability (GI) has been proposed for the massive outer disc regions, especially in the first phases of disc formation (Kratter & Lodato 2016).

However, in the last years, it was shown that non-ideal magnetohydrodynamical (MHD) effects, such as Ohmic and ambipolar diffusion, and the Hall drift, may lead to the quenching of MRI (e.g. the reviews of Turner et al. 2014 and Lesur 2020). First, Gammie (1996) showed that Ohmic resistivity can efficiently suppress MRI in the inner disc mid-plane (dead zone), and proposed that accretion could take place through the MRI-active upper disc layers. Later, Bai (2013) and Bai & Stone (2013) performed local shearing-box simulations of stratified discs where both Ohmic resistivity (dominating in the mid-plane) and ambipolar diffusion (dominating at the surface) were considered, finding that MRI is also quenched in the upper layers of the disc. As a solution to the angular momentum transport problem, these authors revived the old scenario of MHD disc winds, showing that in the presence of a magnetic field with net

★ E-mail: fz258@cam.ac.uk

magnetic flux, accretion is efficiently driven by the launching of a magneto-centrifugal wind. This evidence brought back to popularity the old scenario, first proposed by Blandford & Payne (1982) and Wardle & Koenigl (1993) and revised by Ferreira (1997), that accretion is due to MHD disc winds.

State-of-the-art global simulations, including a realistic treatment of sub-grid micro-physics, confirm these scenarios, showing that, even when all the non-ideal MHD terms are considered, accretion can be efficiently driven by magnetic disc winds (e.g. Bai 2017; Béthune, Lesur & Ferreira 2017; Wang, Bai & Goodman 2019; Gressel et al. 2020). What is more, recent observational results of different kind are also supporting the importance of MHD winds for disc evolution. On the one hand, we have evidence that turbulence is low in the outer disc regions (e.g. Flaherty et al. 2017, 2018, but see Flaherty et al. 2020 for an exception). On the other hand, Atacama Large Millimeter/submillimeter Array (ALMA) observations are also detecting MHD disc wind candidates in molecular lines (e.g. Louvet et al. 2016; Tabone et al. 2017; de Valon et al. 2020; Booth et al. 2021) and forbidden atomic lines (e.g. Fang et al. 2018; Banzatti et al. 2019; Pascucci et al. 2020; Whelan et al. 2021, even though distinguishing between thermal and magnetic winds is not straightforward).

When disc evolution is dominated by MHD winds, *no spreading* is expected because angular momentum is not radially redistributed but removed vertically. This suggests that confronting global disc sizes at different epochs can be a fruitful method to assess if viscosity or winds are the drivers of disc evolution. However, global non-ideal MHD simulations are difficult and numerically expensive to perform because both the large-scale magnetic field and the sub-grid chemistry (to compute the dissipation coefficients) need to be modelled with care and be numerically resolved. Using the results of local simulations, global 1D models can be built (e.g. Armitage, Simon & Martin 2013; Bai 2016; Lesur 2021). Nevertheless, all such models are based on several assumptions owing to their dependence on the simulations to which they were tailored.

Recently, Tabone et al. (2022b) introduced a new simple parametrization of the problem. Following the idea of Suzuki et al. (2016) of applying the parametrization of Shakura & Sunyaev (1973) to magnetic winds, they introduced a coefficient, $\alpha_{\rm DW}$, embodying our ignorance on the magnitude of angular momentum removal by an MHD wind. In addition to Suzuki et al. (2016), Tabone et al. (2022b) were able to find analytical self-similar solutions for wind-dominated discs, analogous to the viscous ones of Lynden-Bell & Pringle (1974) in the viscous case. This makes a large-scale comparison between the two model predictions feasible. In particular, they confirmed the result of Armitage et al. (2013) that in the absence of viscosity no disc spreading takes place.

Since the advent of the ALMA, more and more nearby star-forming regions have been surveyed at low-to-moderate angular resolution (e.g. Ansdell et al. 2016, 2018; Barenfeld et al. 2016; Pascucci et al. 2016), making it possible to compute disc gas and dust sizes for a large number of sources (e.g. Barenfeld et al. 2017; Tazzari et al. 2017; Ansdell et al. 2018; Sanchis et al. 2021). This allows us to compare the different theoretical predictions for disc size evolution with time to data in star-forming regions of different ages in a statistical sense.

Najita & Bergin (2018) were the first to use disc *gas* sizes to search for evidence of viscous spreading between Class 0/I and Class II discs, finding tentative evidence of more evolved discs being larger. However, their sample was non-homogeneous and different molecular tracers (CN and CO, mainly) were used to observationally infer gas sizes. Most importantly, disc sizes measured from CO (sub-)millimetre rotational emission cannot be naively compared to the predictions of viscous evolution, because they are affected by changing physical and chemical conditions over secular timescales. To address this problem, Trapman et al. (2020) built a set of thermo-chemical viscous models taking into account processes such as CO photodissociation, chemical processing (in the warm molecular layer), freeze-out on grains and radial transport, affecting the abundance, distribution and radial extension of CO emission. Their results showed that, when $\alpha_{\rm SS} = 10^{-3}$ and 10^{-4} models and data agree for the young Lupus star-forming region, while for the older Upper Sco OB association, CO sizes were too small for their models (even though no sensitivity cut was considered in the post-processing). Trapman et al. (2022) performed a similar exercise using the magnetic wind models of Tabone et al. (2022b), showing that a good agreement between numerical predictions and data can be seen both in Lupus and Upper Sco. However, magnetic wind models fail at reproducing the disc sizes of younger Class 0/I sources.

In this paper, we follow an alternative approach, and discuss whether disc *dust* sizes can be used as a proxy for disc evolution. This choice can be motivated both by theoretical and observational arguments. In fact, solids dominate ALMA continuum observations, determining the opacity and temperature structure of the disc, and are the key ingredient for planet formation (Birnstiel, Fang & Johansen 2016). Moreover, at the time of writing, gas sizes have been measured only in 35 discs in Lupus (Sanchis et al. 2021) and nine in Upper Sco (Barenfeld et al. 2017), while for dust a larger, homogeneously analysed sample of 30 discs from Lupus, 33 from Chamaeleon I, and 22 from Upper Sco is available (Hendler et al. 2020).

Relying on dust size measurements in the Lupus sample of Ansdell et al. (2016), a tentative evidence of viscous spreading was reported by Tazzari et al. (2017), who showed that Lupus discs were larger than those in the younger Taurus-Auriga and ρ Ophiuchus star-forming regions. However, this trend was not confirmed by Andrews et al. (2018a). When dust is taken into account, several processes come into play that need to be addressed by detailed modelling. In particular, as highlighted by several authors (e.g. Weidenschilling 1977; Takeuchi & Lin 2002; Birnstiel, Dullemond & Brauer 2010; Birnstiel & Andrews 2014; Testi et al. 2014), the dynamics of solids is different from that of the gas because dust is subject to radial drift. Briefly, as a result of the damping effect of the gas, solid particles drift towards the star, with a speed proportional to their size, potentially shrinking the disc dust emission region.

Rosotti et al. (2019b) showed that this is not the case in viscously evolving discs because, promoting the removal of large grains, radial drift becomes 'a victim of its own success'. In fact, once the larger solids are accreted, smaller particles, well coupled with the spreading gas and drifting outwards, determine the overall expansion of the dust disc size with time (when $\alpha_{\rm SS} \gtrsim 10^{-3}$). However, Rosotti et al. (2019b) showed that this trend of increasing dust sizes cannot be seen at the sensitivity of the current population surveys and would be challenging to detect even for much deeper observations.

In this paper, we run 1D gas and dust models, relying on the parametrization of Tabone et al. (2022b) and the simplified treatment of dust growth of Birnstiel, Klahr & Ercolano (2012). Following Rosotti et al. (2019a, b), our aim is to make predictions for the time evolution of the dust disc sizes, assuming that disc evolution is ruled by either viscosity or magnetic winds. We then compare our results with the dust disc sizes inferred from the currently available ALMA observations to determine their agreement and whether this depends on the underlying disc evolution mechanism. We remark that previous works already took into account dust evolution in 1D MHD disc wind models (e.g. Takahashi & Muto 2018; Taki et al. 2021; Arakawa, Matsumoto & Honda 2021, using the prescriptions

of Suzuki et al. 2016 for gas evolution). However, to our knowledge, none of these works focused on disc sizes.

This paper is organized as follows. In Section 2, we introduce our model. Section 3 illustrates our results in a test case. The effects of magnetic winds on dust evolution are discussed, and how they impact the evolution of the mass and flux radius. Section 4 deals with the parameter space exploration, while Section 5 is dedicated to the observational consequences of our work: are current observations able to distinguish between viscous and magnetic-wind evolution, and how our predictions on the correlation between (sub-)millimetre disc sizes and fluxes change with magnetic winds? In Section 6, we discuss possible model limitations. Finally, in Section 7, we summarize our results and draw our conclusions.

2 NUMERICAL METHODS AND OBSERVATIONS

1D simulations of gas and dust evolution are performed using the code developed by Booth et al. (2017). The magnetic wind models of Tabone et al. (2022b) are used for gas, while for dust we employ the simplified treatment of grain growth developed by Birnstiel et al. (2012). The outputs of our simulations are then post-processed to produce synthetic (sub-)millimetre dust observations, to be compared with real data. Hereafter, our numerical methods and observational sample are described.

2.1 Numerical methods

2.1.1 Code architecture

The code implements by default a routine solving the viscous evolution equation (Lynden-Bell & Pringle 1974). This is updated to take into account the effect of magnetic winds as in the master equation of Tabone et al. (2022b, see equation 10, which is written here in the Keplerian case):

$$\frac{\partial \Sigma}{\partial t} = \frac{3}{R}\frac{\partial}{\partial R}\left[R^{1/2}\frac{\partial}{\partial R}\left(\frac{\alpha_{\rm SS}\Sigma_{\rm g}c_{\rm s}^2}{\Omega_{\rm K}}R^{1/2}\right)\right] + \frac{3}{2R}\frac{\partial}{\partial R}\left(\frac{\alpha_{\rm DW}\Sigma_{\rm g}c_{\rm s}^2}{\Omega_{\rm K}}\right) - \frac{3\alpha_{\rm DW}\Sigma_{\rm g}c_{\rm s}^2}{4(\lambda-1)R^2\Omega_{\rm K}}, \quad (1)$$

where we call R the cylindrical radius and t the time variable.

The first term in equation (1) describes how the total disc surface density Σ varies as a consequence of viscous-diffusion processes. Here, $\Sigma_{\rm g}$ is the gas surface density, and viscosity, $\nu = \alpha_{\rm SS}c_{\rm s}^2/\Omega_{\rm K}$, is written according to the Shakura & Sunyaev (1973) prescription. $\alpha_{\rm SS}$ labels the angular momentum transport efficiency due to viscosity, $\Omega_{\rm K}$ is the Keplerian angular velocity, computed for a solar mass star, and $c_{\rm s}$ is the locally isothermal sound speed, which is determined as $c_{\rm s} \propto T^{1/2}$, where T is the disc temperature. In our models, this is set by the stellar irradiation only: as we are interested in the evolution of disc sizes we neglect viscous heating, which is important only in the innermost disc regions. Hence, T is constant in time and decays as $R^{-1/2}$, with $T_0 = 88.23$ K at 10 au, tailored to a solar mass star (Kenyon & Hartmann 1987; Chiang & Goldreich 1997).

The second and third term in equation (1) identify the contribution of magnetic winds to disc evolution. The second term describes the advection of disc gas due to angular momentum removal by magnetic torques associated with acceleration of the wind. In the 'expanded α framework' of Tabone et al. (2022b), this is parametrized similarly to the viscous term: as the viscous accretion rate, $\dot{M}_{\rm acc}^{\rm visc}$, is proportional to $\alpha_{\rm SS}$, so the wind-driven accretion rate, $\dot{M}_{\rm acc}^{\rm wind}$, is proportional to $\alpha_{\rm DW}$, making these two coefficients easy to compare. To first order, $\alpha_{\rm DW}$ is proportional to the disc magnetization, generally denoted by the inverse of the thermal to magnetic pressure ratio in the disc mid-plane, β_0 (Tabone et al. 2022b). The third term identifies the mass-loss rate in the wind, whose impact on disc evolution is described by the magnetic lever arm parameter, λ, defined as the ratio of the angular momentum carried away by the wind along a streamline and at its base (Blandford & Payne 1982).

Equation (1) is solved using finite-differences methods on a grid made up of 4096 cells equally spaced in $R^{1/2}$, between $R_{\rm in} = 10^{-2}$ au and $R_{\rm out} = 10^4$ au. In Appendix A, we show that our code exactly reproduces the analytical self-similar solutions of Tabone et al. (2022b). As initial condition, we consider a tapered power-law profile (Lynden-Bell & Pringle 1974):

$$\Sigma(R, t=0) = \frac{M_0}{2\pi R_0 R}\exp\left(-\frac{R}{R_0}\right), \quad (2)$$

where $M_0 = 0.1\ M_{\rm Sun}$ is the initial disc mass and R_0 is a characteristic radius, initially enclosing 63 per cent of M_0. A proper choice of the initial disc radius is particularly important in magnetic wind models, where gas sizes remain fixed with time (e.g. Armitage et al. 2013; Tabone et al. 2022b). Recent results from CALYPSO (Maury et al. 2019) and VANDAM (Tobin et al. 2020) suggest that disc sizes (estimated from dust emission) in Class 0/I sources are small, with only ≈ 30 per cent of the targets being larger than 50 au.[1] Yet, as Class 0/I discs are actively accreting material from their envelope, their observed sizes do not necessarily give strong constraints on the initial disc radius. For these reasons, following Rosotti et al. (2019b), we set $R_0 = 10,\ 30$, and 80 au.

2.1.2 Parameter space exploration

Our aim is to make predictions of how the observed disc sizes change as a function of the wind intensity. This is described by the parameter $\psi = \alpha_{\rm DW}/\alpha_{\rm SS} \approx \dot{M}_{\rm acc}^{\rm wind}/\dot{M}_{\rm acc}^{\rm visc}$, which quantifies the relative strength of the wind to viscous torque. While we can think of $\alpha_{\rm DW}$ as being dependent on β_0, the value of ψ will depend on the configuration of the magnetic field (bipolar for MHD disc winds) and the disc micro-physics (that tells us if MRI can be triggered), but not necessarily on the disc magnetization. When $\psi = 0$, equation (1) reduces to the viscous evolution equation, while when $\psi \to \infty$ magnetic winds dominate accretion. A fair comparison between models with different ψ requires consideration of discs evolving on the same initial time-scale:

$$t_{\rm acc,0} = \frac{R_0^2}{3\alpha c_{\rm s}^2/\Omega_{\rm K}}, \quad (3)$$

where $\alpha = \alpha_{\rm SS} + \alpha_{\rm DW}$ is the total angular momentum transport efficiency in the disc. When $\psi = 0$, $t_{\rm acc,0}$ is the initial viscous time-scale, $t_{\nu,0}$.

In the following, we consider models with radially homogeneous $\alpha_{\rm SS}$ (resulting in $\nu \propto R$) and $\alpha_{\rm DW}$, for different values of ψ, corresponding to purely viscous evolution ($\psi = 0$), the MHD wind dominated case ($\psi = 10^4$), and a hybrid scenario ($\psi = 1$). In

[1] It is unclear how dust and gas sizes are related in such young sources. However, Class 0 disc observations show that evidence of Keplerian rotation on scales larger than 50 au is rare (2/16 targets in the CO and SO line PDBI/CALYPSO observations of Maret et al. 2020).

a similar exercise in the viscous-only case, Rosotti et al. (2019b) considered $\alpha = 10^{-4}$, 10^{-3}, 10^{-2}, encompassing the typical range bounded by hydrodynamical instabilities to MRI, and $\alpha = 0.025$, for illustrative purposes (and here motivated by the recent detection of high levels of turbulence in DM Tau; Flaherty et al. 2020). The lower values of viscosity are also compatible with the results of Trapman et al. (2020), who modelled CO disc sizes in Lupus, and those of Rosotti et al. (2019a) and Zormpas et al. (2022), for the size–luminosity correlation. We retain the same values of α for an easier comparison of our results with those in the literature. This choice is also motivated by the currently available upper limits on the magnetic field strength (Vlemmings et al. 2019; Harrison et al. 2021), which cannot be used to significantly constrain $\alpha_{\rm DW}$ according to the present theoretical models. For reference, our choice of temperature implies that $t_{\rm acc,0} \approx 0.48$ Myr at $R_0 = 10$ au for $\alpha = 10^{-3}$.

For each ψ and α, we also explore different values of the magnetic lever arm parameter, $\lambda = 1.5$, 3. These are justified by recent observations of disc molecular outflows (e.g. Louvet et al. 2018; de Valon et al. 2020; Booth et al. 2021, where $1.5 \lesssim \lambda \lesssim 2.3$). We remark that this parameter does not set the disc evolution time-scale (equation 3); instead it controls the amount of mass removed by the wind rather than accreted.

Tabone et al. (2022b) also considered models with a time-increasing $\alpha_{\rm DW}$, inversely proportional to the disc mass (corresponding to a locally constant B_z, rather than β_0). In a companion paper, Tabone et al. (2022a) also showed that this solution reproduces the correlation between protoplanetary disc accretion rates and masses inferred from (sub-)millimetre fluxes in Lupus (Manara et al. 2016; Lodato et al. 2017; Rosotti et al. 2017), as well as the decline of the disc fraction with cluster age (e.g. Fedele et al. 2010). For this reason, we take into account the non-constant $\alpha_{\rm DW}$ scenario as well. It is discussed in Section 6, because its results are very similar to the constant $\alpha_{\rm DW}$ case when $\psi \to \infty$, as long as the disc lives long enough.

2.1.3 *Dust evolution*

The code implements the two population model of dust growth developed by Birnstiel et al. (2012) because it has the advantage of closely reproducing the results of full coagulation simulations (Brauer, Dullemond & Henning 2008; Birnstiel et al. 2010) at a much lower computational cost. In summary, two populations of solids are considered: one is made of small, monomer-sized grains ($a_0 = 10^{-5}$ cm, constant in time and space), the other is composed by large grains dominating the mass. Their size, the maximum grain size, $a_{\rm max}$, changes with time as the disc evolves and is set at any radius by the combination of growth (with maximally efficient sticking, $f_{\rm grow} = 1$; Booth & Owen 2020), fragmentation (assuming $u_{\rm f} = 10\,{\rm m\,s^{-1}}$ as velocity threshold for shattering, typical of ice-coated grains; e.g. Gundlach & Blum 2015) and drift. In particular, after an initial phase of growth, $a_{\rm max}$ is determined by either the *turbulent* fragmentation limit, $a_{\rm frag} \propto \Sigma_{\rm g}/\alpha_{\rm SS}$, or the drift limit, $a_{\rm drift} \propto \Sigma_{\rm d}$, whichever is the smallest (Birnstiel et al. 2012):

$$a_{\rm max} = \min\left\{a_{\rm drift},\, a_{\rm frag},\, a_0 \exp\left(t\epsilon\Omega_{\rm K}\right)\right\}, \tag{4}$$

where ϵ is the dust-to-gas ratio. From the previous expressions, it is clear that the most important parameter in determining the grain size is the *viscous* $\alpha_{\rm SS}$ parameter, because this sets the level of turbulent relative velocities that limit grain growth by fragmentation. Interestingly, the wind-dominated disc evolution scenario provides a physically motivated application of previous works (e.g. Pinilla, Lenz & Stammler 2021) studying dust evolution when the global angular momentum transport is decoupled from turbulence on a small scale. We refer to Birnstiel et al. (2012) for further details and to Booth et al. (2017) for the implementation.

Table 1. Summary of the model parameters, references can be found in the text. When a range of parameters is explored, the values used in our test case in Section 3 are boxed.

Parameter	Value
Torque ratio, ψ	0, 1, 10^4
Lever arm parameter, λ	[3], 1.5
Accretion efficiency, α	10^{-4}, [10^{-3}], 10^{-2}, 0.025
Accretion time-scale, $t_{\rm acc}$	4.872, [0.487], 0.048, 0.019 Myr
Initial disc radius, R_0	[10], 30, 80 au
Disc mass, M_0	0.1 $M_{\rm Sun}$
Stellar mass, M_*	1 $M_{\rm Sun}$
Reference temperature, T_0	88.23 K
Dust material density, $\rho_{\rm s}$	1 g cm^{-3}
Fragmentation velocity, $u_{\rm f}$	10 m s^{-1}
Initial grain size, a_0	10^{-5} cm
Initial dust-to-gas ratio, ϵ	10^{-2}
Coagulation efficiency, $f_{\rm grow}$	1

Once the grain sizes are known, they are used to compute the dust velocities of both particle species as in Tanaka, Himeno & Ida (2005) and advect dust along the gas flow. To do so, the dust fraction is updated according to the one-fluid approach of Laibe & Price (2014), assuming that dust is initially distributed as the gas and 100 times less abundant (as in the ISM; e.g. Bohlin, Savage & Drake 1978). The code allows to take into account the back reaction of the dust on the gas (e.g. Dipierro et al. 2018; Gárate et al. 2020). However, this is likely unimportant given that the dust fraction decreases fast due to the efficient radial drift of solids (Rosotti et al. 2019b).

In this paper, dust entrainment in the wind is neglected based on previous works showing that only small grains can be efficiently removed in MHD winds (e.g. Giacalone et al. 2019; Rodenkirch & Dullemond 2022). We discuss this assumption more extensively in Section 6.

Dust diffusion is also considered. The original code implements a diffusion coefficient $D = \nu/{\rm Sc}$, where Sc is the dust Schmidt number, computed as in Youdin & Lithwick (2007). To avoid non-smooth (numerical) features in the purely magnetic case, where viscosity is negligible, we prescribe $D = (\psi + 1)\nu/{\rm Sc}$, so that there is a fixed relationship between angular momentum transport efficiency and diffusivity, regardless of the mechanism for angular momentum transport. Although we do not expect angular momentum transport due to magnetic winds to contribute to turbulent diffusion of solids, their mixing efficiency remains uncertain. Furthermore, the latter choice does not change our results on dust disc sizes.

As a summary of the previous paragraphs, the parameters used in our models are reported in Table 1. The values employed in the test case of Section 3 are boxed.

2.1.4 *Post-processing and disc size determination*

The outputs of our simulations are post-processed to generate synthetic observations at ALMA wavelengths. To do so, we first compute the surface brightness radial profile, $S_{\rm b}$, at $\nu \approx 352.7$ GHz (≈ 0.85 mm, ALMA Band 7) and $\nu \approx 96.7$ GHz (≈ 3.10 mm, ALMA

Band 3) as:

$$S_{\rm b}(R) = B_\nu(T)\left\{1 - \exp\left(-\kappa_\nu \Sigma_{\rm d}\right)\right\}, \quad (5)$$

where $\Sigma_{\rm d}$ is the dust surface density, B_ν is the blackbody radiation spectrum at temperature T, and κ_ν is the dust (absorption) opacity, computed as in Rosotti et al. (2019b), following Tazzari et al. (2016). We refer to Rosotti et al. (2019a) for comments on this choice of opacity. For simplicity, we assume discs to be face-on, which is a fair approximation within a factor $\langle \cos i \rangle = \pi/4 \approx 0.8$ from the average disc inclination on the sky.

In this paper, we consider smooth discs (i.e. continuous, without sub-structures), where defining a characteristic scale radius is arbitrary. A possible solution naturally comes from our parametrization of the initial conditions in equation (2), where the scale radius, R_0, allows to infer how big a disc is. Although this definition naively applies only at the very beginning of the disc life, it can be extended to later times and regardless of the shape of the disc surface density. For example, following Rosotti et al. (2019b), this can be done cumulatively defining as disc radius the location in the disc enclosing a given fraction of the total disc mass. For consistency with the physical interpretation of R_0, we define the *disc mass radius*, $R_{63,\rm mass}$, as the disc size enclosing 63 per cent of the total gas or dust mass, whichever tracer is considered. As this metric is not observationally accessible, we also define an observational *disc flux size* as the radius enclosing a given fraction of the disc luminosity, $R_{x,\rm flux}$. Typical values of x employed in the literature are 68 and 95 per cent (e.g. Tripathi et al. 2017; Andrews et al. 2018a; Manara et al. 2019; Hendler et al. 2020; Sanchis et al. 2021; Tazzari et al. 2021a). Rosotti et al. (2019b) suggested that $R_{68,\rm flux}$ indicates the location in the disc where grains are about the size of the observational wavelength (or the *opacity cliff*, as named by Rosotti et al. 2019b). $R_{95,\rm flux}$, instead, is likely a proxy for the outer disc radius, observationally set by the survey sensitivity.

2.2 Observational sample

To test the viscous and magnetic evolution model predictions, we compare our synthetic disc sizes with those observationally inferred from Lupus (Ansdell et al. 2016), Chamaeleon I (Pascucci et al. 2016; Long et al. 2018a), and Upper Sco (Barenfeld et al. 2016) ALMA data in Band 7. We mainly refer to the work of Hendler et al. (2020), who computed dust disc sizes homogeneously among these regions, and use the PPVII Chapter table of Manara et al. (2022), who adopted *Gaia*-EDR3 distances (Gaia Collaboration 2021). We choose these star-forming regions because they are among the best studied nearby ones, with high levels of completeness and disc detection fractions. Moreover, they span a wide age range: Lupus ($\approx$ 1–3 Myr; Comerón 2008), Chameleon I ($\approx$ 2–3 Myr; Luhman et al. 2008), Upper Sco ($\approx$ 5–10 Myr; Preibisch et al. 2002). This is ideal to test our model predictions over a long-time interval. In Table 2, we summarize the main properties of the data sets taken into account.

We also compare the behaviour of our models with Lupus and Upper Sco data in the disc size *versus* luminosity plane. We use the sizes and fluxes computed by Hendler et al. (2020) from ALMA Band 7 data and those derived by Tazzari et al. (2021a) from ALMA Band 3 (Tazzari et al. 2021b) data in sub-sample of Lupus discs.

3 RESULTS IN A TEST CASE

We discuss the impact of magnetic winds with different mass-loss rates on dust evolution in a test case with $\alpha = 10^{-3}$ and $R_0 = 10$ au. Then, the evolution of the mass radius and flux radius is detailed.

Table 2. Size properties of the Lupus (Ansdell et al. 2016), Chamaeleon I (Pascucci et al. 2016; Long et al. 2018a), and Upper Sco (Barenfeld et al. 2016) samples taken into account: number of observed discs, discs where sizes were measured and resolved, median and 1σ uncertainty of $R_{68,\rm flux}$ for resolved discs only. Data on measured and resolved discs are from Hendler et al. (2020). Note that the *Gaia*-corrected median distances for resolved discs are in line with those reported by Hendler et al. (2020).

Region	Observed	Measured	Resolved	$R_{68,\rm flux}$
Lupus	89	50	30	$46.82^{+45.52}_{-30.88}$
Chamaeleon I	93	58	33	$32.49^{+35.70}_{-8.81}$
Upper Sco	106	44	22	$25.05^{+15.58}_{-12.37}$

3.1 Dust evolution in the test case

Fig. 1 compares dust evolution profiles at different times in viscous and magnetic wind models. The radial profiles of the dust surface density, $\Sigma_{\rm d}$, dust-to-gas ratio, ϵ, and maximum grain size, $a_{\rm max}$, are displayed from top to bottom and each column highlights models with different torque ratios: from left to right, the viscous evolution case ($\psi = 0$, bench-marked against Rosotti et al. 2019b results), the hybrid scenario ($\psi = 1$) and the purely magnetic wind case ($\psi = 10^4$).

Let us first focus on the viscous case (left-hand panel): the main features of dust evolution were already discussed in previous works (e.g. Birnstiel et al. 2012; Rosotti et al. 2019b) and are briefly summarized hereafter:

(i) dust depletes very fast and by $t = 3$ Myr the dust-to-gas ratio falls below $\epsilon = 10^{-5}$;
(ii) initially dust growth is limited by fragmentation in the inner disc and by dust drift in the outer disc: the transition between the two regimes is identified by the kink in the dust-to-gas ratio profiles (see dots in Fig. 1). The drift-dominated regime encompasses larger disc regions with time;
(iii) the dust surface density displays a sharp outer edge at any time (Birnstiel & Andrews 2014). This is determined by the abrupt change in dust velocity at these locations.

We can discuss now how these characteristics change when discs evolve under the effect of magnetic winds. As can be seen from Fig. 1, in the purely magnetic wind case (solid lines in the right-hand panel), dust growth is limited only by radial drift and no kink in the dust-to-gas ratio can be seen. This happens because, at fixed α, the magnetic wind models have lower levels of viscosity. Therefore, no *turbulent* fragmentation takes place, and the disc is drift-dominated throughout. What is more, discs also lose solids faster: dust masses are 50 times smaller than in the purely viscous case, after $t = 3$ Myr, when $\psi = 10^{-4}$. A possible explanation is as follows. In the absence of winds, because of viscous spreading, small grains well coupled with the gas can migrate outwards. Those grains make up a reservoir of solids that grow, decouple from gas and eventually drift on very long time-scales, replenishing the inner disc with dust at later times. In the purely magnetic wind case, instead, no outward diffusion is possible and the solids sink (faster) on the star as dust velocities are directed inwards at any radius, causing the disc outer edge to move accordingly. Similar results were described by Sellek, Booth & Clarke (2020a) in the case of discs evolving under the effect of external photoevaporation and by Zagaria, Rosotti & Lodato (2021) for discs in binary systems.

In the hybrid case (solid lines in the central panel), an intermediate behaviour is present. Because of the reduced contribution of viscosity to the angular momentum transport, discs become drift-dominated

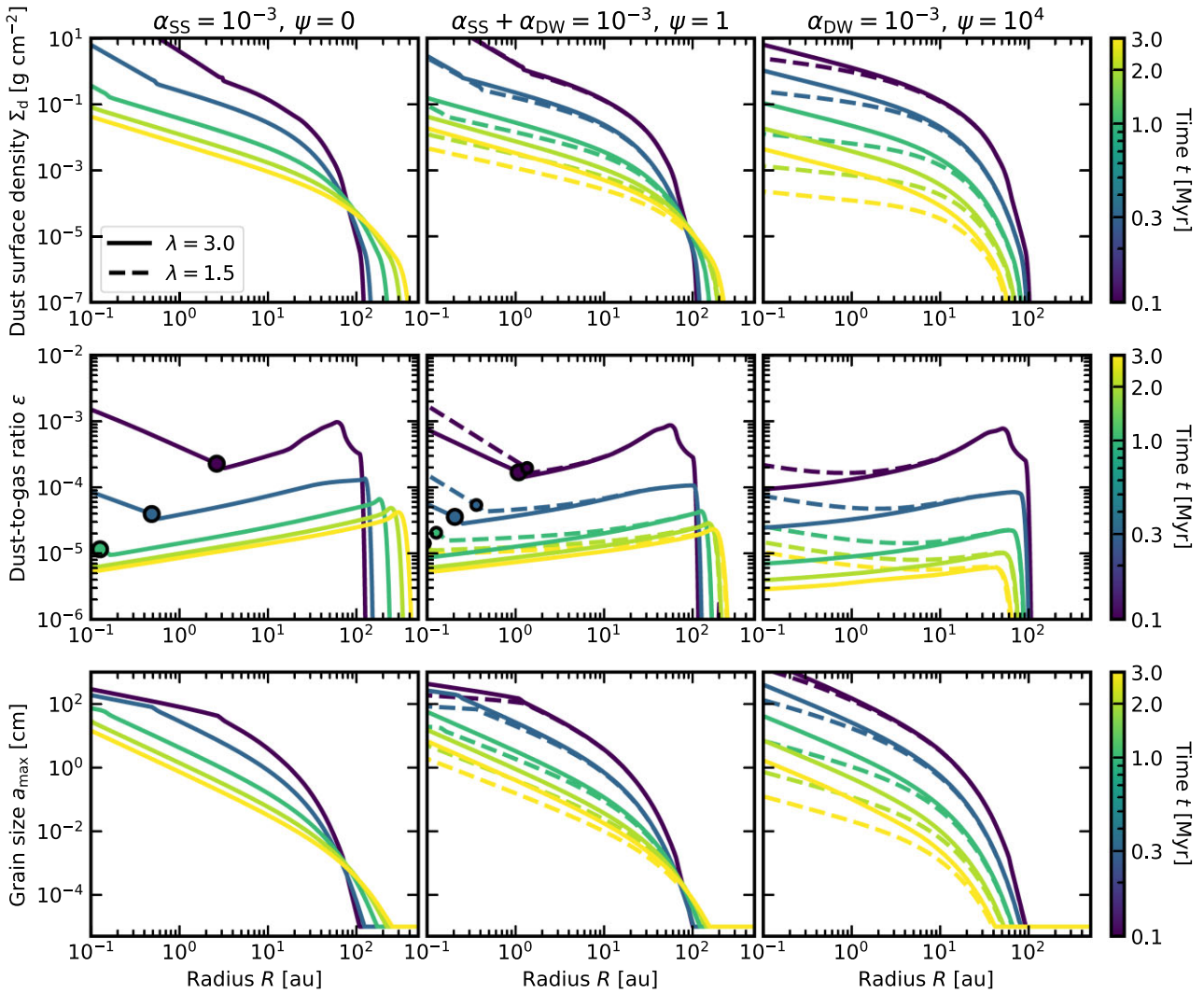

Figure 1. Upper panels: Dust surface density radial distribution for different disc evolution models in the test case ($\alpha = 10^{-3}$, $R_0 = 10$ au). From left to right: viscous evolution ($\psi = 0$), hybrid case ($\psi = 1$), magnetic wind evolution ($\psi = 10^4$). Solid lines are used for moderate mass-loss rates ($\lambda = 3$), while dashed lines for less-efficient winds ($\lambda = 1.5$). Middle panels: Dust-to-gas ratio radial distribution. Dots mark the transition between fragmentation-dominated and drift-dominated dust regime, larger for $\lambda = 3$ and smaller for $\lambda = 1.5$. Bottom panels: Maximum grain size radial distribution.

at a factor of 2 to 3 smaller radii, but fragmentation is still important in the inner disc. Dust masses are three times smaller than in the purely viscous case, after $t = 3$ Myr, but not as low as in the purely magnetic wind case because a small amount of spreading is present.

In Fig. 1, we also consider the effect that changing the lever arm parameter has on dust evolution. The solid lines discussed so far refer to the $\lambda = 3$ case, while the dashed lines are used for models with $\lambda = 1.5$. In this case, when discs are dominated by MHD winds the dust surface density and the maximum grain size rise less strongly in the inner disc because the gas surface density is shallower in the same regions ($\Sigma_d^2 \propto \Sigma_g / \Omega_K R^2$ in the drift-dominated regime, and $a_{drift} \propto \Sigma_d$; see Birnstiel et al. 2012). In the hybrid model, the transition between fragmentation-dominated and drift-dominated regions of the disc moves to larger radii. This can be explained on account of the higher dust-to-gas ratio in the inner disc ($a_{drift}/a_{frag} \propto \epsilon$), motivated by the larger gas loss with respect to the $\lambda = 3$ case (see also discussion in Tabone et al. 2022a). Finally, although the (locally) larger dust-to-gas ratio may hint at the expectation that more dust is retained when $\lambda = 1.5$, these models lose two to three times more solids than in the case of $\lambda = 3$. This is due to the faster velocity of grains, which decouple earlier from the gas because of the lower gas surface density.[2]

3.2 Dust disc sizes in the test case

Our models are evolved from 0 to 3 Myr. In the following, we consider how their characteristic sizes change after every 5×10^4 yr snapshot. In Fig. 2, the dust mass radius and the 68 and 95 per cent flux sizes at 352.7 GHz (i.e. 0.85 mm, ALMA Band 7), are plotted as a function of the disc age for different values of ψ. Solid and dashed lines display $\lambda = 3$ and 1.5 models, respectively.

Let us consider the $\lambda = 3$ case first. In the left-hand panel of Fig. 2, we can see that magnetic winds substantially affect the mass

[2]This dominates over the change of surface density slope in the inner disc, which has the opposite effect of reducing the dust velocity, that is proportional to the local pressure gradient (Brauer et al. 2008).

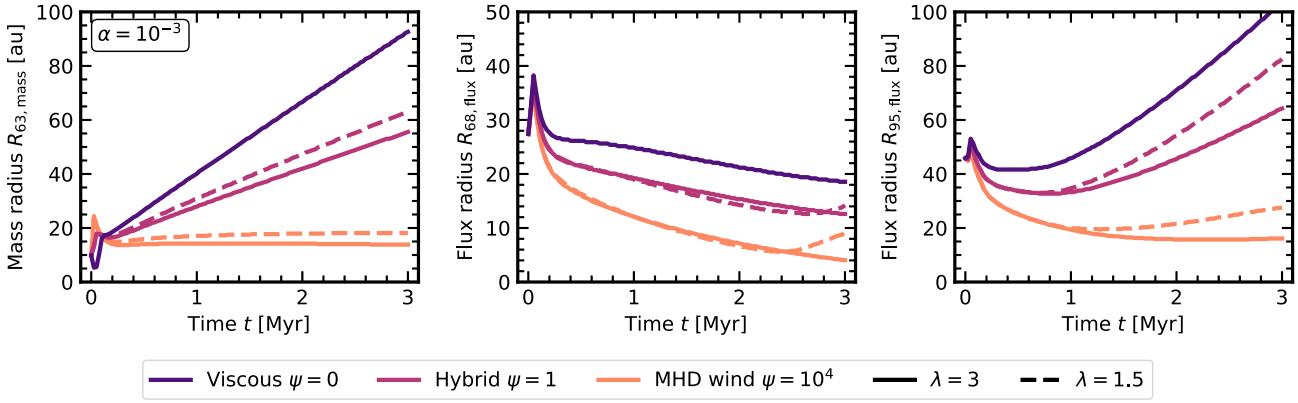

Figure 2. From left to right: dust mass radius and 68 and 95 per cent flux sizes as a function of the disc age for different evolution models. Solid and dashed lines display $\lambda = 3$ and 1.5 models, respectively.

radius evolution. While in the viscous model, $R_{63,\mathrm{mass}}$ increases with time, this is not always true when magnetic winds are considered. In particular, the higher ψ is, the less the mass radius grows. Eventually, in the purely magnetic wind case, after an initial transient determined by the removal of large dust (Rosotti et al. 2019b), $R_{63,\mathrm{mass}}$ remains steady. This is due to the absence of viscous spreading that allows for small, well-coupled grains to move to larger and larger radii, increasing the mass radius. In fact, by $t = 3$ Myr, the purely MHD wind model is smaller than the purely viscous one by a factor of 5.

While the behaviour of the mass radius is insensitive to its definition ($R_{x,\mathrm{mass}}$, with $x \in [50, 100]$), this is not true for the flux radius. On the one hand, as is shown in the central panel of Fig. 2, $R_{68,\mathrm{flux}}$ always decreases with time, regardless of ψ. On the other hand, in the right-hand panel of Fig. 2, we can see that $R_{95,\mathrm{flux}}$ closely follows the behaviour of the mass radius: it increases the most in the viscous case and remains steady in the purely magnetic wind model.

Moving to the $\lambda = 1.5$ case, it can be seen from Fig. 2 that the absolute values of the disc sizes are sensitive to the magnetic lever arm parameter. Specifically, they are larger for smaller values of λ, as can be understood by the less steep dust surface density in this case. Nevertheless, variations are small, usually within 20 to 30 per cent. Most importantly, the increasing/decreasing trend of the disc sizes is not influenced by the lever arm parameter.[3] This is why in the following we will only consider the $\lambda = 3$ case and move to Appendix B a discussion on how our results change when $\lambda = 1.5$.

4 PARAMETER SPACE EXPLORATION

In this section, we discuss the behaviour of the mass and flux radius for different values of ψ, as a function of the initial disc size, R_0, and angular momentum transport efficiency, α.

4.1 The evolution of the mass radius

Fig. 3 displays the evolution of the mass radius for different initial parameters. In each sub-plot, solid lines are used for the dust, dashed lines for the gas, colour coded according to the initial disc radius, R_0. Different values of α and ψ are used, moving from the top to the bottom along a column and from the left to the right along a row, respectively.

4.1.1 *Dependence on the initial radius*

Let us first focus on the viscous evolution models ($\psi = 0$) with $\alpha = 10^{-3}$. As already discussed in the previous section and in Rosotti et al. (2019b), $R_{63,\mathrm{mass}}$ increases with time, and is larger for a larger R_0. When the disc scale radius is big enough, an initial transient (peak) can be seen. This is an effect of grain growth and radial drift. (i) First, the large and fast growing particles in the inner disc are removed ($R_{63,\mathrm{mass}}$ increases). (ii) Then, the grains drift as they grow also in the outer disc regions ($R_{63,\mathrm{mass}}$ decreases). (iii) Finally, when only the smallest, well-coupled grains are left, the mass radius expands again. As discussed in Rosotti et al. (2019b), this effect is more evident for a larger R_0 because of the longer evolution timescales, implying a slower growth, drift, and outward diffusion of solids at large radii.

When magnetic winds dominate disc evolution ($\psi > 0$), similar behaviours with R_0 can be observed. However, $R_{63,\mathrm{mass}}$ increases less or remains steady because of the reduced viscosity contribution to angular momentum transport.

4.1.2 *Dependence on α*

Let us first focus on the viscous evolution models ($\psi = 0$). When $\alpha = 10^{-4}$, viscosity is so low that no late time expansion can be observed, regardless of R_0. For this reason, no differences can be noticed with the magnetic wind cases.

For a larger α, the models undergo two expansion phases (Rosotti et al. 2019b). For $\alpha = 10^{-2}$, the mass radius initially grows slowly, then substantially expands because grains become smaller and well coupled with the gas (corresponding to the bulk of the disc transitioning from the fragmentation-dominated to the drift-dominated regime). In this case, $R_{63,\mathrm{mass}}$ can be larger for a smaller initial radius, because grains become drift-dominated earlier. Instead, when $\alpha = 0.025$, after expanding with the gas, the dust radius grows less than the gas radius because of the small grains in the outer disc decoupling from the gas and drifting inwards.

In the purely magnetic wind models ($\psi = 10^4$), the mass radius follows a completely different evolutionary path. After an initial transient, which can be motivated as in the previous paragraphs, $R_{63,\mathrm{mass}}$

[3] In the purely magnetic wind models, at late times $R_{68,\mathrm{flux}}$ and $R_{95,\mathrm{flux}}$ increase when $\lambda = 1.5$. This is because the brighter inner disc shrinks so much that the fainter regions out of the *opacity cliff* become significant to the total disc luminosity (Sellek et al. 2020a; Toci et al. 2021). This takes place earlier for $\lambda = 1.5$ than for $\lambda = 3$ because of the faster removal of the grains with size beyond the cliff.

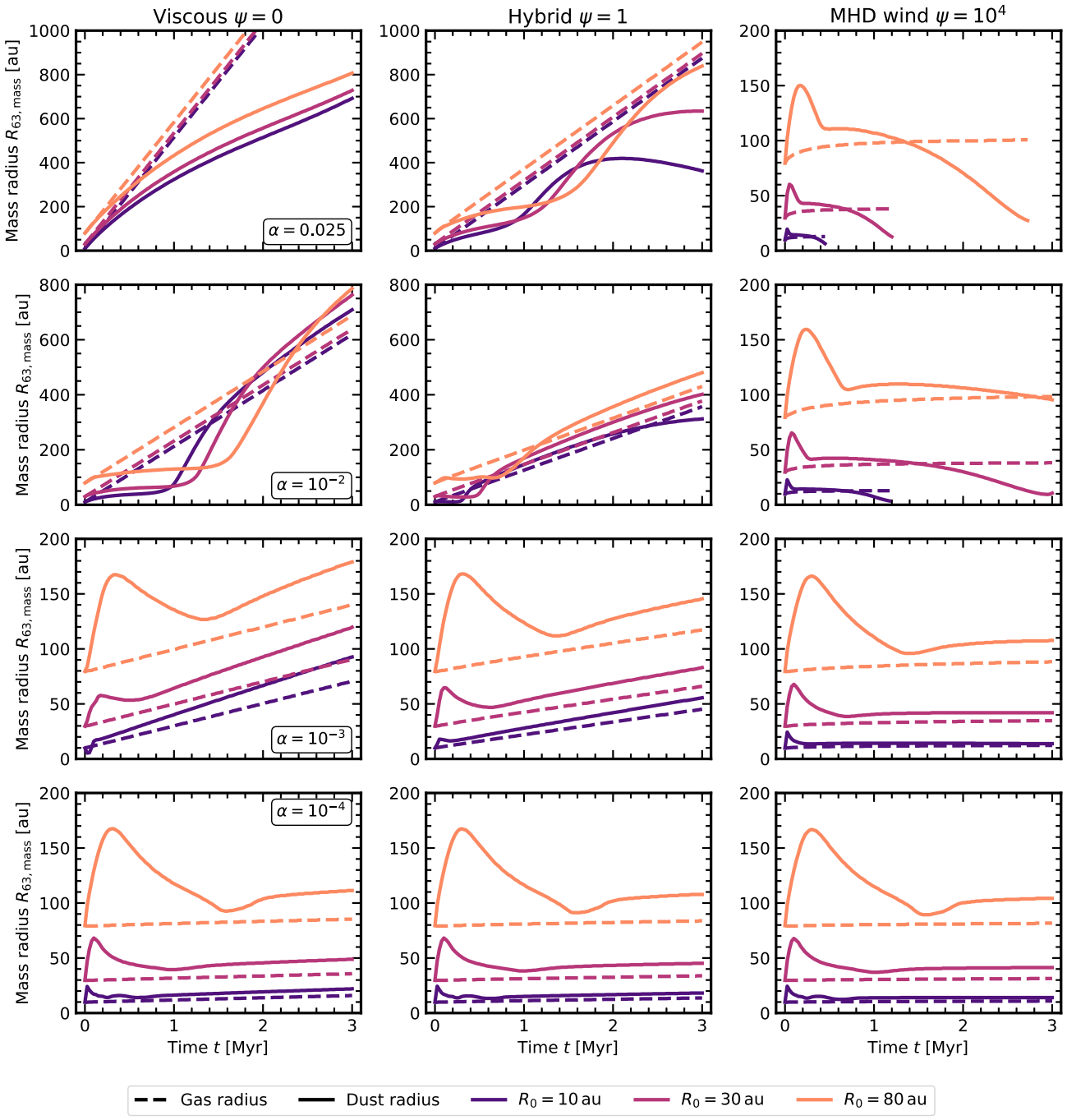

Figure 3. Mass radius for gas (dashed lines) and dust (solid lines) time evolution as a function of α (row by row) and ψ (column by column), for $\lambda = 3$.

stays constant or decreases, and eventually plummets, because of the fast drift of solids. This process takes place at different characteristic times: earlier for a larger α (because of the faster evolution) and a smaller R_0 (because of the faster dust removal). For $\alpha = 10^{-2}$ and 0.025, we decided to plot the mass radius evolution up to the time-step when all the large grains are removed as the disc would be dispersed by this stage (when the track is ended the highest measured dust mass in our models is $\approx 4 \times 10^{-5}\ M_{\mathrm{Jup}}$, about the mass of the Moon, and generally 10^3 times smaller). $R_{63,\mathrm{mass}}$ then rapidly increases and finally attains the same value as in the gas (not shown).

Finally, in the hybrid models ($\psi = 1$), for both $\alpha = 10^{-2}$ and 0.025, the behaviour of $R_{63,\mathrm{mass}}$ resembles the viscous case with $\alpha = 10^{-2}$, as can be expected by the reduced turbulence in hybrid models. However, the late stages of evolution are characterized by a moderate disc shrinkage as the small particles in the outer disc decouple from the gas and drift inwards. For lower values of α, an intermediate behaviour between the viscous and purely MHD wind case can be seen.

4.1.3 Dust-to-gas size ratio

Finally, we comment on the relationship between dust and gas radii. In the viscous scenario, gas sizes always expand, while in the wind-dominated case they remain steady (Armitage et al. 2013; Tabone

et al. 2022b). Dust disc sizes are larger or smaller than the gas ones depending on the steepness of the dust surface density with respect to the gas surface density.[4] The latter is given by $-1+\xi$ (Tabone et al. 2022b), where $\xi = \mathrm{d}\log \dot{M}_{\rm acc}^{\rm wind}/\mathrm{d}\log R$ (Ferreira & Pelletier 1995) is known as the ejection index. The former is mainly determined by the mechanisms that set the grain size in the disc. Adopting the same method of Birnstiel et al. (2012), but see also the analytical solutions of Birnstiel & Andrews (2014), it can be shown that in the fragmentation-dominated regime $\Sigma_{\rm d} \propto R^{-3/2}$, steeper than the gas, while in the drift-dominated one $\Sigma_{\rm d} \propto R^{(-3+2\xi)/4}$, which is always less steep than the gas for $\lambda = 3$.

To sum up, in the viscous evolution models the dust mass radius always expands as long as viscosity is large enough ($\alpha \gtrsim 10^{-3}$). Generally speaking, larger initial sizes and a larger α lead to larger discs. In the purely magnetic wind scenario, instead, the dust mass radius stays constant when the rate of angular momentum extraction in the wind is low ($\alpha \lesssim 10^{-3}$). However, for stronger winds, $R_{63,\rm mass}$ decreases and solids rapidly disperse.

4.2 The evolution of the flux radius

In Fig. 4, the evolution of the 68 and 95 per cent flux radius at 352.7 GHz (i.e. 0.85 mm, ALMA Band 7), is shown in dashed and solid lines, respectively.

Regardless of ψ, for $\alpha \lesssim 10^{-3}$, the 68 per cent flux radius decreases with time because the grains with the largest opacity ($a_{\rm max} \approx 0.02$ cm, corresponding to the *opacity cliff* size) in the inner disc drift towards the star. Instead, when $\alpha \gtrsim 10^{-2}$, after an initial shrinking phase, $R_{68,\rm flux}$ can get larger with time in the viscous and hybrid cases. This happens because the 68 per cent flux radius is not tracing the disc region where $a_{\rm max}$ is about the observational wavelength. In fact, the contribution of small grains ($a_{\rm max} \lesssim 0.02$ cm, below the *opacity cliff*) to the disc brightness becomes important in this case, because the larger particles were already removed. Moreover, $R_{68,\rm flux}$ has a similar time-dependence as the mass radius.[5]

The 95 per cent flux radius closely follows the behaviour of the mass radius. When angular momentum transport is negligible ($\alpha = 10^{-4}$), after an initial shrinking phase due to the brightest grains drifting inwards (corresponding to the transient in the mass radius and enhanced by opacity effects), it remains steady. A similar initial decrease can be observed for $\alpha = 10^{-3}$, with $R_{95,\rm flux}$ eventually growing in the viscous and hybrid models and remaining steady in the purely magnetic wind case. When $\alpha \gtrsim 0.01$, no shrinking is observed in the viscous and hybrid cases, because dust and gas are well coupled. As a consequence, the 95 per cent flux radius increases, until the small grains in the outer disc start drifting efficiently (e.g. $\psi = 1$, $\alpha = 0.025$, $R_0 = 10$ au, where $\Sigma_{\rm d}$ drops and the solids become drift-dominated). On the contrary, in the purely magnetic wind scenario, the 95 per cent flux radius never grows as expected from the absence of outwards disc spreading.

In our experiments, we also considered different definitions of the observed dust disc sizes, $R_{x,\rm flux}$, using intermediate flux percentages, x, between 68 and 95. However, these quantities are not useful to distinguish MHD wind and viscous evolution, because their ability to recover viscous expansion depends on α.

To sum up, radial drift leads the central brightest region of the disc to shrink, regardless of the evolutionary scenario. Nevertheless, when sufficiently large fractions of the dust flux are used to define disc sizes, we recover the same behaviour of the mass radius. This is due to the faint outer disc expanding in viscous and hybrid models. Thus, the 95 per cent flux radius is a promising proxy to distinguish viscous/hybrid evolution from the purely MHD wind one.

5 OBSERVATIONAL CONSEQUENCES

In this section, we discuss our model prediction for the evolution of observed dust disc sizes and the size–luminosity correlation. Then, the results of our synthetic observations are compared with real data in Lupus, Chamaeleon I, and Upper Sco.

5.1 Can observations discriminate between viscous and wind-driven evolution?

Although the 95 per cent flux radius is a promising proxy for viscous expansion as opposed to magnetic wind shrinking or stalling, it was already highlighted by Rosotti et al. (2019b) that measurements of viscous spreading are expected to be challenging even for ALMA.

Current surveys are not deep enough to distinguish between viscous and wind-driven evolution. To motivate this statement, following the argument of Rosotti et al. (2019b), we repeat our calculation of the flux radius neglecting dust emission falling below the sensitivity threshold given by $S_{\rm b,0.85mm} \approx 6 \times 10^7$ Jy sr^{-1}, corresponding to ≈ 2 min integration time and 0.3 arcsec angular resolution observations, similar to those of Ansdell et al. (2016), Barenfeld et al. (2016), and Pascucci et al. (2016). The new sizes are shown in Fig. 5 as dashed lines. $R_{95,\rm flux}$ always decreases regardless of the model parameters, making it impossible to distinguish between viscous and magnetic wind models. Noticeably, however, purely magnetic wind models with $\alpha \gtrsim 10^{-2}$ would be already dispersed by this time, reducing the parameter space for comparing dust disc sizes among different disc evolution models to $\alpha \approx 10^{-3}$ to 10^{-4}.

As shown by Rosotti et al. (2019b), deeper observations (e.g. with a sensitivity threshold of $S_{\rm b,0.85mm} \approx 1 \times 10^6$ Jy sr^{-1}) can approximately recover the theoretical values with no sensitivity cut, hence the different evolutionary trend for dust disc sizes in the viscous and magnetic case. This is displayed in Fig. 5 in solid lines. However, achieving these high sensitivity is possible either drastically reducing angular resolution (1 arcsec for 1 h integration time) or through prohibitively long surveys (0.67 arcsec for 5 h integration time), as discussed in Rosotti et al. (2019b). In the first case, which is the most feasible for observations involving more than one source, angular resolution would be enough only for viscous and hybrid models with $\alpha \geq 10^{-2}$ to be resolved at the distance of nearby star-forming regions ($d \approx 140$ au). In fact, these are the only models reaching dust disc sizes of more than 200 au after 1 Myr of evolution. Magnetic wind models, instead, would either disperse or be too small to be resolved. This suggests that very compact/unresolved discs (making up between 50 and 60 per cent of the Lupus population, according to Miotello et al. 2021), detected with very high sensitivity, could

[4]Our result of dust disc sizes being larger than gas disc sizes can be counter-intuitive. Indeed, the latter are generally predicted (Facchini et al. 2017; Trapman et al. 2019; Toci et al. 2021) and observed (Ansdell et al. 2018; Facchini et al. 2019; Andrews 2020; Sanchis et al. 2021; Miotello et al. 2022) to be larger than the former. However, our results are not necessarily in tension with the literature, because they are based on the total gas *mass*, rather than the CO *flux*. A proper comparison with the observations would require modelling CO emission, which is beyond the aims of this paper.

[5]Once a disc is mainly made of small grains, it is reasonable to assume that it is optically thin. Then $S_{\rm b} \propto T\kappa_\nu \Sigma_{\rm d}$, and the surface brightness changes with time as the dust surface density does, because very small grains have a uniform opacity and the temperature does not vary with time in our models.

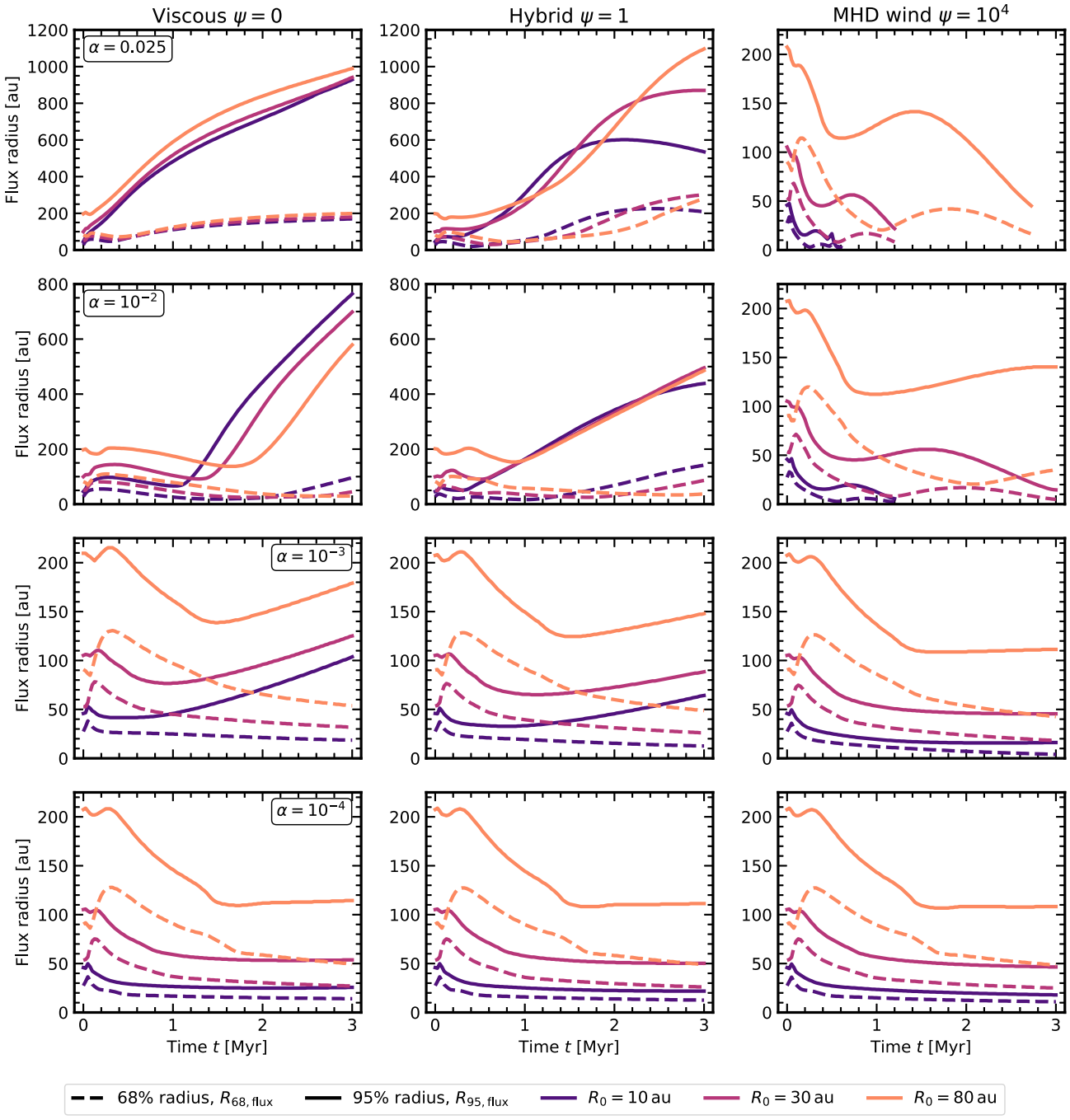

Figure 4. 68 per cent (dashed lines) and 95 per cent (solid lines) flux radius time evolution as a function of α (row by row) and ψ (column by column), for $\lambda = 3$.

be evolving under the effect of magnetic winds.[6] However, at the limited sensitivity of current surveys, it is also possible that those discs looking compact are instead larger and faint in their outer regions.

The case of $\alpha = 10^{-3}$ shows the most striking differences between viscous and (non-dispersing) magnetic wind models. However, these discs would perhaps be too small to be resolved by ALMA in the configuration with high sensitivity and shortest integration time discussed in the previous paragraph. On top of this, the initial decrease in $R_{95,\mathrm{flux}}$ would make it difficult to assess if viscous expansion is actually taking place (Rosotti et al. 2019b). A possible solution to this problem is provided by considering the evolution of disc sizes between star-forming regions with a larger age difference.

We evolve our models with $\alpha = 10^{-3}$ from 0 to 10 Myr and consider how their characteristic sizes change after every 1×10^5 yr snapshot. In Fig. 6, the same exercise as in Fig. 5 is repeated for these longer lived models. As can be seen, viscous expansion can be recovered if observations are deep enough. On the contrary,

[6]In the case of Lupus or Chamaeleon external processes reducing disc sizes such as photoevaporation and tidal truncation due to fly-bys can be neglected.

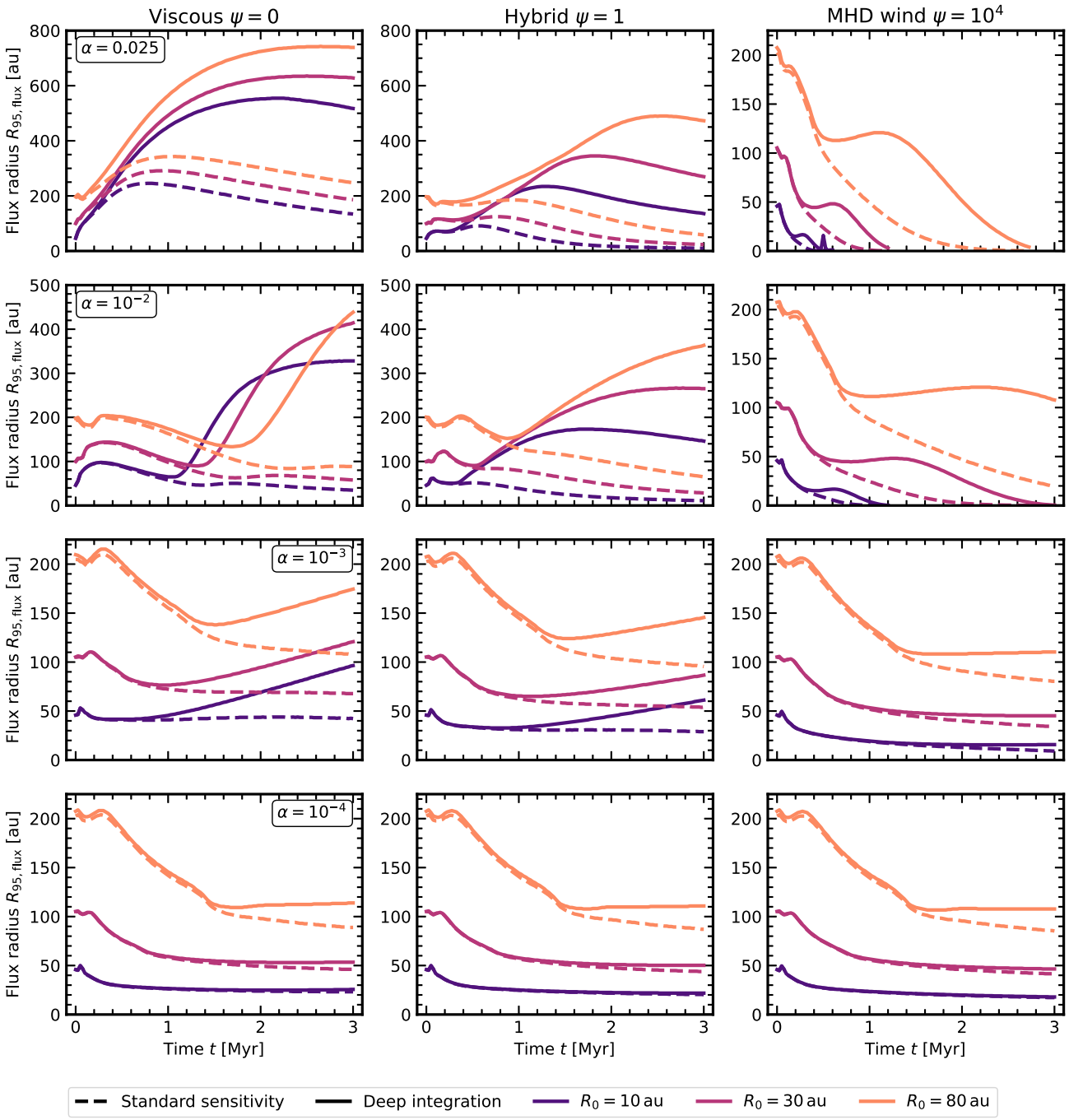

Figure 5. 95 per cent flux radius time evolution as a function of α (row by row) and ψ (column by column), for $\lambda = 3$. The current survey case and the deep sensitivity scenario are plotted as dashed and solid lines, respectively.

wind-dominated models have constant sizes. Furthermore, these differences are still observable considering disc sizes enclosing down to 85 per cent of the disc luminosity, which would be more observationally feasible and lead to more robust results. However, models of long-lived discs require a proper treatment of late time dispersal (e.g. photoevaporation), which is expected to complicate this picture. We refer to Section 6 for a proper discussion.

In summary, current observations cannot distinguish between viscously evolving or wind-dominated disc models. In the case of deeper observations, viscous/hybrid models are characterized by dust disc sizes increasing over time, while purely MHD wind ones either shrink and disperse or stay the same. Even in this case, data sets with large age differences are required for a fruitful comparison.

5.2 Comparison between the observationally inferred dust disc sizes and our model predictions

We compare dust disc sizes inferred from synthetic observations with those homogeneously computed by Hendler et al. (2020) and Manara et al. (2022). We restrict to the case of $\alpha = 10^{-3}$ and 10^{-4}, because only in these cases purely magnetic wind models retain enough dust by 10 Myr. Note that, this choice is also in line with

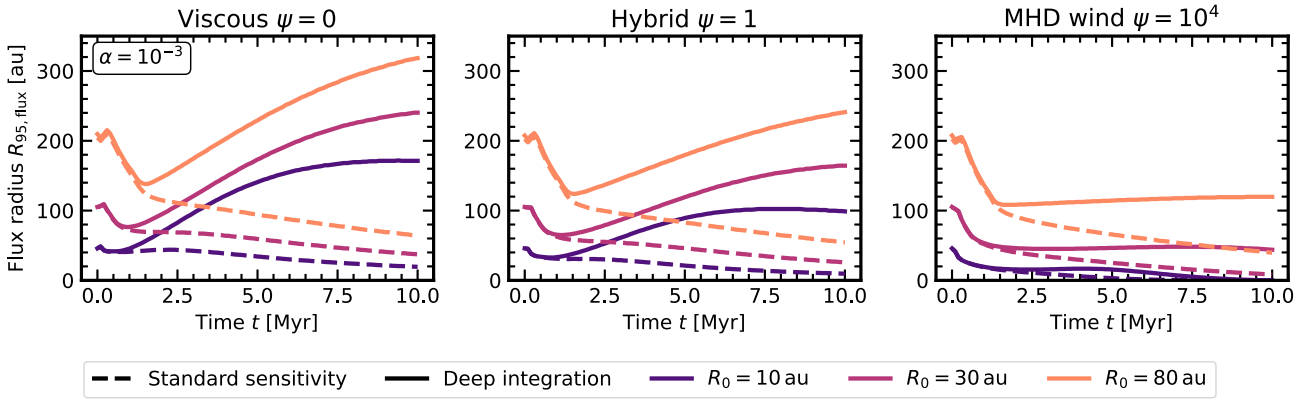

Figure 6. Same as in Fig. 5 for models with $\alpha = 10^{-3}$ evolving up to 10 Myr: deep integration is required to discriminate wind-driven and turbulent accretion.

the observed mass accretion rates in T Tauri discs (e.g. Lodato et al. 2017; Sellek, Booth & Clarke 2020b). Then, the median $R_{68,\mathrm{flux}}$ is computed over the time corresponding to the average age of each star-forming region, for different values of the initial disc radius and ψ, neglecting dust emission below $S_{\mathrm{b},0.85\mathrm{mm}} \approx 6 \times 10^7$ Jy sr^{-1}.

Fig. 7 shows the results of our comparison. Observed discs *with resolved sizes* are displayed as black and grey dots for Lupus, Chamaeleon I, and Upper Sco. To avoid all, the discs in each star-forming region to fall on the same position along the x axis, we use the `swarmplot` function in the `python` data visualization library `seaboarn`, which prevents them from overlapping. In addition, to give a flavour of the tentative underlying disc size distribution in each star-forming region, we draw a violin plot within the range of the observed data. Instead of showing discrete bins (e.g. histograms), `seaborn.violinplot` uses a Gaussian kernel to produce a continuous size distribution (known as kernel density estimation). The median of the data and their 16th and 84th percentiles are also indicated by the dashed and dotted lines in each violin plot. The median of the models is overplotted using squares for $\alpha = 10^{-3}$ and dots for $\alpha = 10^{-4}$, with error bars displaying their 16th and 84th percentiles, obtained from the size evolution within the region age, colour coded by their initial disc radius as in the previous plots.

As expected from the discussion so far, the theoretical predictions are very similar for all the models shown in Fig. 7, yet some differences can be highlighted. On the one hand, viscous models with both $\alpha = 10^{-3}$ and 10^{-4} are broadly compatible with the data. The predicted sizes are somewhat at the lower end of the observed distributions, but generally within 1σ about the median of the data. On the other hand, magnetic wind models are more dependent on the α. When $\psi = 10^4$, for $\alpha = 10^{-3}$ (squares) discs initially larger than 30 au are required to match the bulk of Lupus and Chamaeleon I data. As for Upper Sco, only initial sizes of around 80 au are compatible with the median of the observed distribution. Instead, for $\alpha = 10^{-4}$ the agreement improves at the age of Upper Sco, giving results similar to the viscous model ones, as expected from the reduced viscosity. Larger sizes for smaller α is counter-intuitive based on our previous discussion. However, this happens only by the age of Upper Sco when fewer large grains are retained in models with larger α, which are evolving (and dispersing) faster.

In the purely magnetic wind scenario, models with $R_0 < 30$ au are smaller than all the observed discs. However, this is not necessarily something to worry about because only resolved discs are plotted in Fig. 7. These correspond to about a third of the disc-bearing young stellar objects with detected (sub-)millimetre emission in each of the star-forming regions taken into account, and are those in the upper-end of the size and luminosity distribution (Hendler et al. 2020). We expect that higher resolution observations would mitigate this bias, decreasing the median observed size, in better agreement with magnetic wind models with small R_0.

5.2.1 *Comments on sub-structures*

None of the models can predict dust disc sizes large enough to reproduce the observed discs with $R_{68,\mathrm{flux}} \gtrsim 65$ au. A naive solution is that of increasing R_0, but this would be at odds with the measured sizes of Class 0/I discs (see Section 2). More likely, discs could be larger because sub-structured.

The advent of ALMA has made it possible to detect a number of sub-structures in discs that were previously thought to be smooth (see Andrews 2020 for a recent review). The Disk Substructures at High Angular Resolution Project (DSHARP; Andrews et al. 2018b) and the unbiased survey of Long et al. (2018b) in Taurus supported the popular hypothesis of sub-structures being common. Nevertheless, no conclusive answer has been given in the case of fainter/smaller discs (Long et al. 2019).

Gaps and cavities, in particular, are expected to perturb the otherwise smooth and radially decreasing disc pressure profile, creating local enhancements where particles get trapped and pile up (Whipple 1972; Pinilla et al. 2012). The presence of sub-structures can thus affect the dust disc size evolution, because the particle radial motion is halted. However, both the extent and outcome of this process are difficult to predict because they depend on several parameters (e.g. the gap location, width, number, and their ability to retain grains of different sizes for long time; see e.g. Pinilla, Pascucci & Marino 2020; Zormpas et al. 2022). These questions will be addressed in future works.

For the time being, Fig. 7 distinguishes between smooth discs, plotted as black dots, and sub-structured ones, shown in grey. Interestingly, lots of these have dust disc sizes much larger than those predicted by our models. However, while in Lupus we find 15 discs with sub-structures (van der Marel et et al. 2018; Andrews et al. 2018b; van der Marel et al. 2018), only two were detected in Chamaeleon I (Pascucci et al. 2016) and Upper Sco (Barenfeld et al. 2016; Andrews et al. 2018b), because of the different angular resolution of this surveys (and follow-up ones, e.g. more Lupus discs are in DSHARP; Andrews et al. 2018b). Given the limited number of detected gaps in the oldest region, the extent to whom sub-structures modify our dust disc size predictions can be assessed only partially.

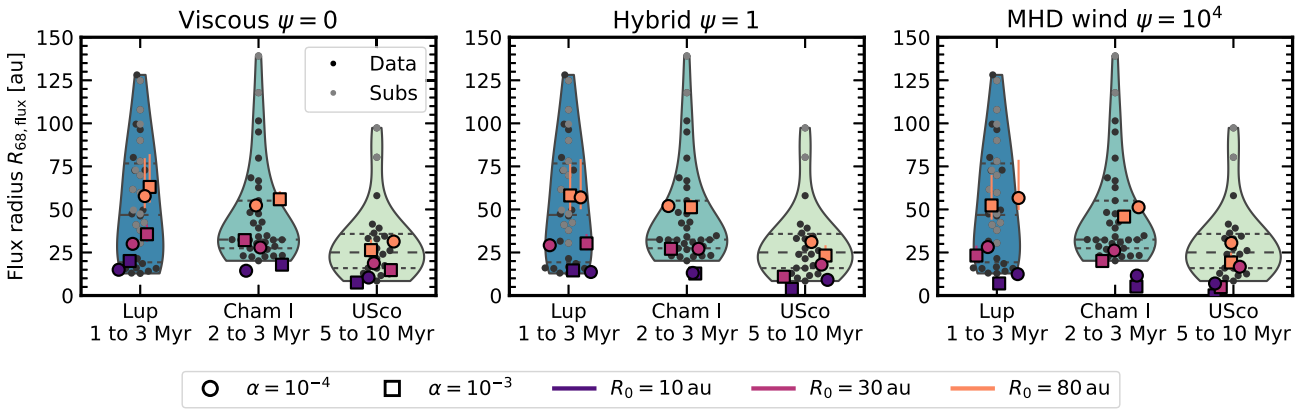

Figure 7. 68 per cent flux radius for Lupus (Lup), Chamaeleon I (Cham I), and Upper Sco (USco) discs in black (and grey when sub-structured). Dashed and dotted lines in the violin plot indicate the median of the data and their 16th and 84th percentiles. Large squares and dots display the median of the models with $\alpha = 10^{-3}$ and 10^{-4}, respectively, and $\lambda = 3$, colour coded by R_0 (see legend). Error bars show their 16th and 84th percentiles.

5.2.2 Longer wavelengths

Recently, Tazzari et al. (2021b) published a catalogue of Lupus discs observed with ALMA in Band 3 (3.10 mm). These targets are among the brightest sources observed by Ansdell et al. (2016, 2018) in Band 6 and 7 (1.33 mm and 0.89 mm). In a companion paper, Tazzari et al. (2021a) showed that these sources have comparable sizes in all the three bands, with the median $R_{68,\mathrm{flux}}$ decreasing less than 10 per cent over the explored wavelength range.

This trend is not consistent with our smooth viscous nor magnetic disc models. In fact, we find that the 68 per cent flux radius generally follows the position in the disc where the dust grains are about the size of the observational wavelength, which Rosotti et al. (2019b) called the *cliff radius*. For longer wavelengths, the cliff radius moves inwards in the disc, because it is attained at larger grain sizes. For this reason, we expect $R_{68,\mathrm{flux}}$ to decrease significantly with wavelength, as opposed to what observed by Tazzari et al. (2021a).

This trend for $R_{68,\mathrm{flux}}$ being wavelength-independent is observed regardless of the presence of resolved sub-structures, suggesting that it is not due to discs being 'truncated' by an outer disc gap (so that $R_{68,\mathrm{flux}}$ follows the location of the outermost gap). Thus, as suggested by Tazzari et al. (2021a), a possible solution comes from hypothesizing that *unresolved* dust traps could be ubiquitously present in the sample, explaining why large grains are retained at large radii, at odds with our models.

To conclude, regardless of ψ, models generally predict disc sizes in good agreement with those measured in Band 7, with the exception of purely magnetic wind models with a small initial radius. However, the presence of sub-structures halting the radial motion of the solids can impact our results. Our work needs to be re-assessed when enough higher resolution data on smaller/fainter and sub-structured discs will be available, in particular at the age of Upper Sco, when the models differ the most.

5.3 The size–luminosity correlation

In Figs 8 and 9, we compare models and observations in the disc dust size, $R_{68,\mathrm{flux}}$, and luminosity, $L_{\mathrm{mm}} = F_\nu \times (d/140\,\mathrm{pc})^2$, plane.

A correlation between dust disc sizes and disc luminosities ($R_{68,\mathrm{flux}} \propto L_{\mathrm{mm}}^{\alpha}$ with $\alpha \approx 0.5$ to 0.6) was first detected in bright Taurus discs at 0.89 mm by Tripathi et al. (2017) using SMA data. This correlation was later confirmed by Andrews et al. (2018a) in a larger sample including Lupus discs and by Barenfeld et al. (2017) in Upper Sco using a different procedure. More recently, Hendler et al. (2020) studied the correlation in star-forming regions of different ages homogeneously computing dust disc sizes and luminosities. They showed that the slope of the correlation is not universal and gets flatter (and more tentative) in Upper Sco ($\alpha \approx 0.22$).

The size–luminosity correlation was originally explained as due to discs being either marginally optically thick, with an average optical depth fraction of 0.3 (Tripathi et al. 2017; Andrews et al. 2018a) or by the effect of dust self-scattering on fully optically thick discs (Zhu et al. 2019). Alternatively, Rosotti et al. (2019a) suggested that a quadratic relation between disc fluxes and sizes naturally emerges when radial drift is the main limiter of grain growth. More recently, Zormpas et al. (2022) proposed that both large sub-structured discs and small and smooth sources, where grain growth is limited by radial drift, are needed to account for the entire Lupus population. Hereafter, we explore how our models behave in the disc size *versus* disc luminosity plane and how they compare with the observations. In particular, we are interested in whether a correlation exists between sizes and luminosities and how this changes with the torque ratio, the age of the region and the observational wavelength.

In Fig. 8, the flux radius, $R_{68,\mathrm{flux}}$, is plotted as a function of the disc luminosity, L_{mm}, for different values of ψ after a sensitivity cut at $S_{\mathrm{b,0.85mm}} \approx 6 \times 10^7\,\mathrm{Jy\,sr^{-1}}$. Models between 1 and 3 Myr are compared with Lupus data, while models between 5 and 10 Myr are compared with Upper Sco data, in the top and bottom panels, respectively. Solid, dashed, and dotted lines identify the evolutionary tracks with increasing values of α. Observations are shown as blue dots for Lupus and green dots for Upper Sco; downward-pointing triangles of the same colours are used for disc size upper limits. The data were taken from Hendler et al. (2020) and Manara et al. (2022). The observed correlations and their 1σ scatter are displayed as grey dash–dotted lines and shaded areas. The best-fitting values are from Hendler et al. (2020).

Let us first focus on the top left panel where viscous models are compared with Lupus data. As shown by Rosotti et al. (2019a), simulations with low α (solid and dashed lines) can reproduce the slope of the observed correlation because radial drift is the main mechanism limiting grain growth. However, when $\alpha = 10^{-2}$ (dotted lines), dust is fragmentation-dominated and $R_{68,\mathrm{flux}}$ does not scale as a power law of the disc luminosity, in contrast with the bulk of the observations. Overall, our models reproduce the correlation normalization slightly worse than those in Rosotti et al. (2019a), which were a factor of 2 colder than ours at any given radius. In fact,

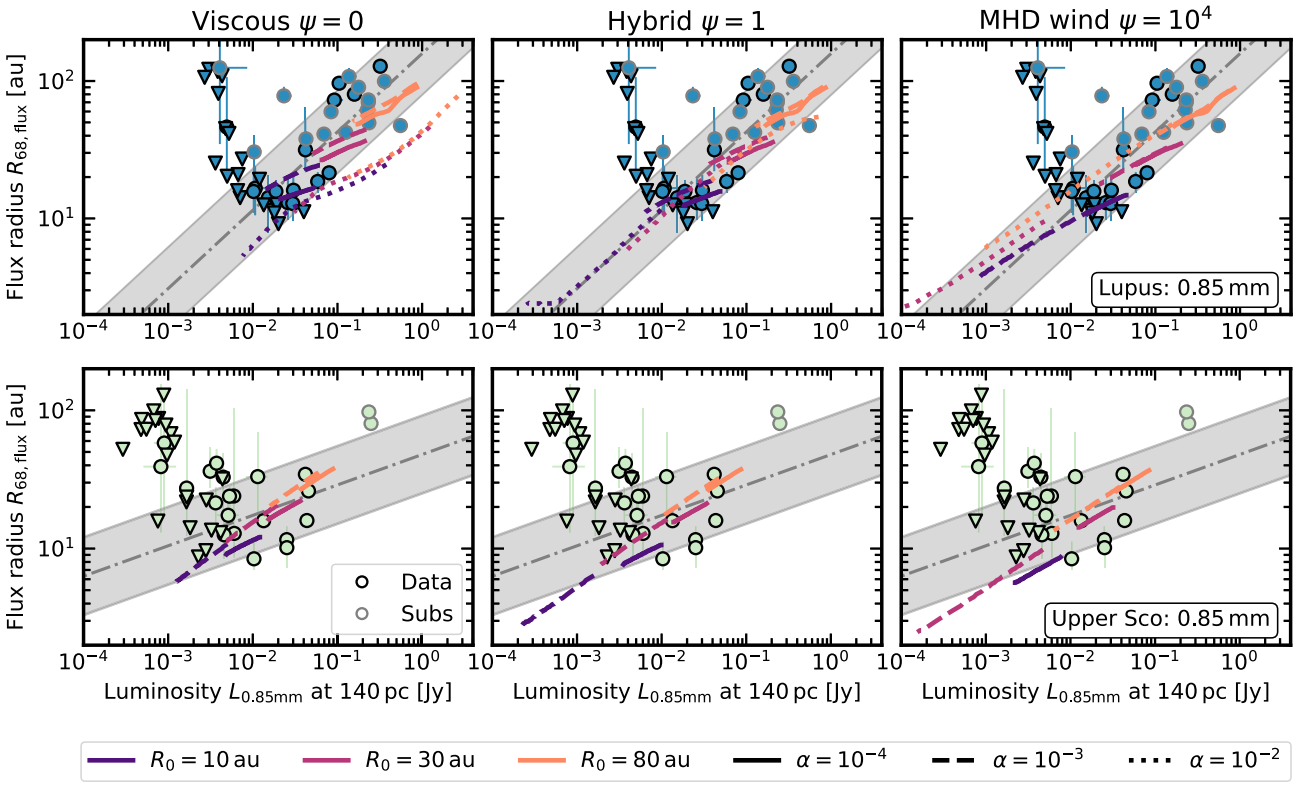

Figure 8. ALMA Band 7 size–luminosity correlation in Lupus (top row) and Upper Sco (bottom row) as a function of ψ. Solid, dashed, and dotted lines display the evolutionary tracks for increasing values of α, colour coded according to R_0. The grey dash–dotted lines and shaded areas display the observed correlations and their 1σ spreads, respectively. Data are shown as blue dots for Lupus and green dots for Upper Sco, downward-pointing triangles of the same colours are used for upper limits on the disc sizes. Grey contours are used for discs with detected sub-structures.

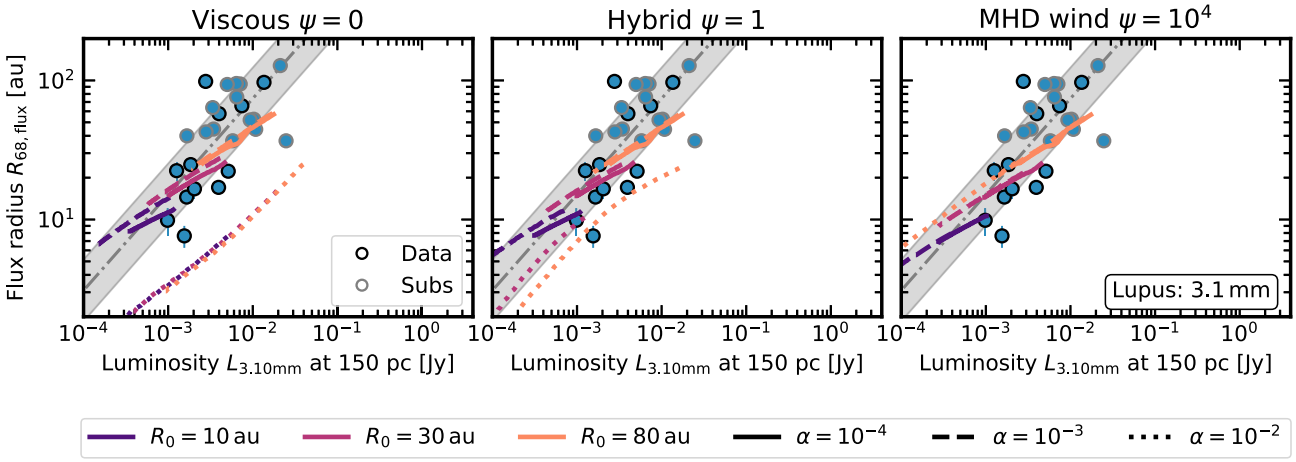

Figure 9. Same as in Fig. 8 for ALMA Band 3 size–luminosity correlation in Lupus.

several sources have luminosities $\leq 0.2 L_{\mathrm{Sun}}$, while our temperature profile was tailored to a Sun-like star. Furthermore, as highlighted by Zormpas et al. (2022), also the assumed opacity model is crucial for the correlation normalization. Some discs have larger sizes than in our models. This was already expected from Fig. 7 and can be due to sub-structures halting radial drift. Sub-structured discs are shown in Fig. 8 with a grey edge and partially confirm the previous hypothesis. Several sources have undetected sizes, challenging the comparison between models and data.

Similar considerations are also valid for the hybrid and purely MHD wind models. These span larger areas of the parameter space, down to $\approx$10 times lower sizes. This is particularly clear for $R_0 = 10$ au models, as expected from Fig 7. An important difference with the viscous case arises when $\psi = 10^4$: the slope of the size–luminosity correlation is reproduced by $\alpha = 10^{-2}$ models as well. This is because in the wind-dominated models grain-growth is limited by radial drift (see the test case in Section 3) also for larger values of α.

Hendler et al. (2020) computed homogeneously fluxes and sizes of discs in star-forming regions of different ages, showing that the slope of the size–luminosity correlation is not universal. This is not seen in our models between 5 and 10 Myr, displayed in the

bottom panels of Fig. 8. Here, the evolutionary tracks have very similar slopes to those in younger models between 1 and 3 Myr. This is clearly in contrast with the observed size–luminosity relation.[7] Nevertheless, we remark that the correlation in Upper Sco is still tentative and needs better observations to be confirmed. In particular, it is possible that several unresolved discs with large upper limits on their dust sizes contribute to flatten the correlation. Our models can reproduce some of the observed sources in the small size range, regardless of the mechanism ruling the transport of angular momentum.

5.3.1 Longer wavelengths

Tazzari et al. (2021a) compared sizes and luminosities at different wavelengths for a sample of Lupus discs among the brightest in the sample of Ansdell et al. (2016, 2018). They found that a correlation is present at 0.89, 1.33, and 3.10 mm, but its normalization and slope increase with wavelength. Similarly to Fig. 8, Fig. 9 displays the size–luminosity correlation for different values of ψ in ALMA Band 3. After a sensitivity cut at $S_{\rm b,3.10mm} \approx 1 \times 10^7$ Jy sr^{-1} (corresponding to an integration time of 2 min and an angular resolution of 0.35 arcsec as in the configuration used for the 18 brightest sources in the sample of Tazzari et al. 2021b), our models between 1 and 3 Myr are compared with Lupus data (Tazzari et al. 2021a, b).

As can be seen, the slope of the models is very similar to the one in Fig. 8. Indeed, under the assumption that the flux radius correlation is driven by the grains being in the drift regime, Rosotti et al. (2019a) showed that changing the observational wavelength only affects the correlation normalization that is expected to increase proportionally to the wavelength squared. However, in the data, the correlation slope is slightly different[8] between the two bands: ≈0.57 to 0.61 in Band 7 (Hendler et al. 2020; Tazzari et al. 2021a) and ≈0.69 in Band 3 (Tazzari et al. 2021a), potentially because of the absence of faint discs in the sample of Tazzari et al. (2021b). Most importantly, our models are smaller than roughly half of the sources in Tazzari et al. (2021a), several of which show evidence of sub-structures, as already highlighted in the previous sub-section.

To sum up, viscous and magnetic wind models behave similarly in the size–luminosity plane and can explain the observed correlation when they are in the drift-dominated regime. However, the non-universality of the correlation slope in the data and the presence of discs too large for our models suggest that the correlation is not only/primarily shaped by the process controlling grain-growth (e.g. radial drift). Sub-structures trapping solids efficiently could be a possible explanation for these discrepancies as is discussed in Zormpas et al. (2022), both in the viscous and MHD-wind case.

[7]Interestingly, purely magnetic wind models with $\lambda = 1.5$ can reproduce the slope of the correlation at the age of Upper Sco, because they have similar sizes as in the case with $\lambda = 3$ but much lower disc fluxes, which tilts the tracks to lower slopes.

[8]Recently, Zormpas et al. (2022) published a more comprehensive analysis of the size–luminosity correlation in Lupus, where they suggested that smooth viscous discs are not consistent with the observed Band 3 correlation. However, Zormpas et al. (2022) compared their results with the correlation coefficients obtained for face-on discs (see Tazzari et al. 2021a). Instead, we use the integrated flux for consistency with Hendler et al. (2020). Interestingly, the largest difference between the correlation slope is obtained in Band 3, where discs are more optically thin than in Band 7 and the effect of the disc inclination should be less important.

6 DISCUSSION

6.1 Grain growth in the absence of turbulence

Our predictions on the secular evolution of dust disc sizes depend on the underlying grain growth model. In fact, the implementation of a full coagulation routine is computationally expensive and prevents the exploration of a large parameter space. For this reason, we adopted the simplified treatment of grain growth provided by Birnstiel et al. (2012), which reproduces the results of more complex calculation but is less time-consuming. This model was benchmarked against a grid of 39 full simulations with $10^{-5} \leq \alpha_{\rm SS} \leq 10^{-3}$. Such a range is consistent with the parameter space we explored in the case of viscous and hybrid models, but not in the purely magnetic wind scenario, where $10^{-8} \leq \alpha_{\rm SS} \leq 10^{-6}$. What is more, Birnstiel et al. (2012) considered turbulence as the main source of particle relative velocities, and hence the driver of grain growth. However, this is not true at the low viscosities considered in our magnetic wind models.

It can be hypothesized that grain growth is inhibited in laminar discs: when only Brownian motion and vertical settling are considered as a source of dust relative velocities, $a_{\rm max} \approx 1$ cm at 1 au after 1 Myr (Safronov 1972; Dullemond & Dominik 2005). Instead, if vertical mixing and turbulent relative velocities are included, $a_{\rm max} \approx 10^4$ to 10^5 cm (Dullemond & Dominik 2005; Brauer et al. 2008). Nevertheless, Brauer et al. (2008) showed that when radial drift and fragmentation are also taken into account, this picture changes. In the turbulent case, the maximum size grains can grow to is dramatically reduced because of destructive collisions between very fast grains, while in the laminar case the differential radial motion becomes an important source of relative particle velocities that allows for coagulation. In the models of Brauer et al. (2008), after 10^4 yr solids are 20 times larger when $\alpha_{\rm SS} = 10^{-10}$ than for $\alpha_{\rm SS} = 10^{-3}$ (see fig. 14 in Brauer et al. 2008), showing that grains can grow also in laminar discs and potentially to larger sizes than in turbulent ones.

Provided that solids can grow in the absence of turbulence, we are confident in the two population predictions in the laminar case. Even though the growth time-scale was not tailored to reproduce the purely magnetic wind scenario, it only influences our results in the very first stages of disc evolution ($t \lesssim 0.1$ Myr), then radial drift becomes the dominant process setting the dust disc sizes.

In the absence of strong turbulence, relative particle velocities are determined by differential radial drift, a mechanism potentially leading to particle fragmentation. Birnstiel et al. (2012) showed that fragmentation by differential drift can be safely overlooked in the outer disc, where the radial drift limit becomes dominant early on. However, when $\alpha_{\rm SS}$ is very low, it can be important in the inner disc. For this reason, fragmentation by differential drift is implemented by default in our code. All in all, it sets the maximum grain size only in the $R \lesssim 1$ au region of the disc when $t \lesssim 1$ Myr, as long as the dust-to-gas ratio is large, $\epsilon \gtrsim 0.0013 \times R^{0.5}$. We conclude, as Birnstiel et al. (2012) did, that this fragmentation mechanism is generally unimportant (but see Pinilla et al. 2021 in the case of lower fragmentation velocities).

6.2 Dust entrainment in magnetic disc winds

MHD disc winds are expected to be strong enough to uplift small dust grains as supported by the evidence of solids in disc outflows (e.g. Bans & Königl 2012; Ellerbroek et al. 2014). The entrainment and thermal processing of dust in magnetic winds has also been proposed as an explanation for the presence of crystalline silicates

in the outer disc, where temperatures are too low for their *in situ* formation through thermal annealing (Salmeron & Ireland 2012; Giacalone et al. 2019).

In our models, however, we neglect dust removal in the wind. This is a reasonable approximation as long as dust particles can grow rapidly to scales that are sufficiently larger than the maximum grain size that can be entrained in the wind, $a_{\rm crit}$. In what follows, we discuss values of $a_{\rm crit}$ from recent literature studies and estimate when the dust mass-loss in the wind can be significant for our results.

Miyake, Suzuki & Inutsuka (2016) first studied dust vertical motion in the presence of magnetic winds, but adopted a fixed background for gas, resulting from previous 3D *local* shearing box simulations. Giacalone et al. (2019), instead, employed *global* steady-state semi-analytical solutions for the gas and also considered dust radial motion. They showed that only dust particles with radius smaller than $a_{\rm crit} \approx 0.1$ to 1 μm can be uplifted by the wind, with ≈ 30 per cent of them re-entering the disc at larger radii. Similar maximum entrained particle sizes were inferred by Rodenkirch & Dullemond (2022), who performed 2D non-ideal MHD simulations employing different dust species.

Nevertheless, $a_{\rm crit}$ scales linearly with the *gas* mass-loss rate in the wind. Giacalone et al. (2019) chose $\dot{M}_{\rm g,w} = 3.5 \times 10^{-8}\, M_{\rm Sun}\, {\rm yr}^{-1}$, corresponding to an implausibly high efficiency wind with $\lambda = 108.4$, and similar values were inferred by Rodenkirch & Dullemond (2022) in discs with warm (i.e. with thermal contributions) and cold (i.e. purely magnetic) winds with $10^4 \leq \beta_0 \leq 10^5$. This suggests that larger grains can be uplifted when the mass-loss rates in the wind are larger, for example, in early disc evolutionary phases (as seen in Miotello et al. 2014 and suggested by Wong, Hirashita & Li 2016).

More recently, Booth & Clarke (2021) modelled the entrainment of dust in ionized winds, showing that it is prompted by the delivery of small grains to the wind base, which is induced by advection in the wind rather than turbulent diffusion. We use the model of Booth & Clarke (2021) to infer the maximum size of grains delivered to the wind in our simulations and estimating the total *dust* mass-loss rate in the wind, $\dot{M}_{\rm d,w}$, as

$$\dot{M}_{\rm d,w} = \int_{R_{\rm in}}^{R_{\rm out}} f\, \dot{\Sigma}_{\rm g,w} \epsilon 2\pi R {\rm d}R. \tag{6}$$

Here, $\dot{\Sigma}_{\rm g,w}$ is the *gas* mass-loss rate in the wind computed as in equation (2), ϵ is the dust-to-gas ratio and f is the fraction of grains entrained in the wind. To compute such fraction, we assume that the number of grains of sizes between a and $a + {\rm d}a$ follows a power-law distribution of the grain size, $n(a){\rm d}a \propto a^{-q}{\rm d}a$, leading to

$$f \approx \min\left[1, \left(\frac{a_{\rm crit}}{a_{\rm max}}\right)^{4-q}\right]. \tag{7}$$

In this work, we assume an MRN distribution (Mathis, Rumpl & Nordsieck 1977), with $q = 3.5$, which is appropriate for a collisional distribution of grains, such as that of small growing dust particles. Nevertheless, using more top-heavy grain size distributions (up to $q = 2.5$), more suitable for dust grains sizes dominated by radial drift (Birnstiel et al. 2012), our results remain similar.

Using equation (6), we can estimate the *dust* mass lost in the wind summing over each simulation time-step. Generally, less than 1 to 2 per cent of the initial dust mass is removed by the wind. Notable exceptions are initially small discs with very strong winds ($R_0 = 10$ au, $\alpha \gtrsim 10^{-2}$, $\lambda = 1.5$), where this fraction can reach 15 to 40 per cent. In such cases, however, a comparison between dust disc sizes in viscous and magnetic wind models on secular time-scales was already prohibitive, because of the very fast dispersal of dust discussed in Sections 4 and 5, in the MHD-wind case.

Using the $a_{\rm crit}$ of Giacalone et al. (2019), almost identical results are obtained. Our inferences refer to the first 3 Myr of disc lifetime but are not expected to change over longer times as the bulk of the grains is removed in the initial time-step ($t \lesssim 2.5 \times 10^4$ yr), where $a_{\rm crit} > a_{\rm max}$ throughout the disc. Finally, it must be mentioned that the grain growth time-scale is crucial for the determination of the dust mass-loss rates in the wind. If grains can grow faster in MHD discs than predicted by the two-population model, our previous estimates are upper limits.

To sum up, we are confident that dust entrainment in MHD winds can be overlooked in those models with $\alpha \approx 10^{-3}$ to 10^{-4} we used to compare disc sizes between viscous and MHD evolving discs.

6.3 Late time dispersal

Discs do not simply fade away with time but are expected to disperse abruptly (e.g. Fedele et al. 2010). In the traditional framework of viscous evolution, photoevaporation has been successfully proposed as an efficient dispersal mechanism because of its possibility to account for the observed inside-out disc clearing (Koepferl et al. 2013). On top of viscous evolution, internal photoevaporation (Clarke, Gendrin & Sotomayor 2001; Owen et al. 2010) brings about a phase of so-called photoevaporation starved accretion (Drake et al. 2009). The disc becomes progressively depleted in the region of maximum wind mass-loss rate (where $R \approx GM_*/c_{\rm s}^2$, roughly at tens of au), then a gap opens further in. The inner disc is viscously drained on the (smaller) gap edge time-scale, while the outer disc is progressively eroded by the wind. We expect photoevaporation to impact disc size evolution as discussed before in the case of gaps, because the wind-opened cavity can retain dust, forming bright rings.

On the contrary, discs evolving under the effect of MHD winds naturally disperse if a dependence of the angular momentum transport coefficient on the disc mass, $\alpha_{\rm DW} \propto M_{\rm disc}^{-\omega}$ with $\omega > 0$, is considered (Tabone et al. 2022b). These models, however, cannot reproduce the inside-out clearing predicted by photometric disc surveys.[9] Mass and flux sizes when $\omega = 1$ are plotted in Appendix C and show very similar results as the purely magnetic wind case with $\omega = 0$ considered so far. In Fig. 10, we test how the dust disc sizes of these models compare with the observations as in Fig. 7. However, here we only consider disc models with $\alpha = 10^{-4}$ at $t = 0$. This is because even for small discs with $R_0 = 10$ au, their dispersion time-scale, $t_{\rm disp} \lesssim 10$ Myr, is long enough for a comparison with Upper Sco discs. As is clear from the plot, $\omega = 1$ models behave as the purely magnetic wind ones (with $\omega = 0$) in Fig. 7: they reproduce well the range of observed sizes within 1σ about the median. Again the largest discs in Hendler et al. (2020) cannot be accounted for by smooth models.

7 CONCLUSIONS

This paper is devoted to making predictions on dust disc sizes and comparing them with the currently available observations in nearby star-forming regions. To do so, we ran a number of 1D gas and dust models with the aim of exploring a large region of the parameter space, varying the angular momentum transport efficiency, α, the

[9] Some models, such as those of Suzuki et al. (2016), predict an inner depletion of the disc, but this outcome depends on the prescription for the wind/disc ionization and is not naturally arising as in the case of photoevaporation.

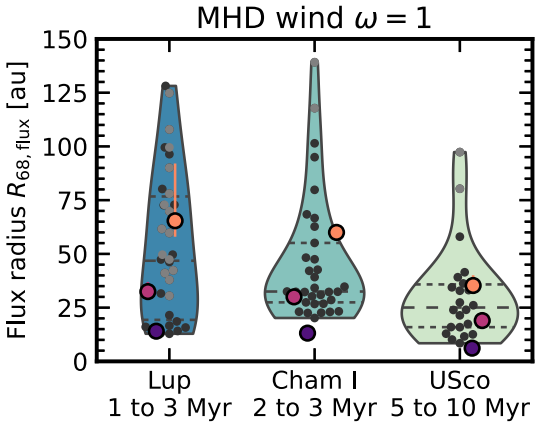

Figure 10. Same as in Fig. 7 for $\omega = 1$ models with $\alpha_{\mathrm{DW}}(t = 0) = 10^{-4}$ and $\lambda = 3$.

torque ratio, ψ, the initial scale radius, R_0, the lever arm parameter, λ, and the dependence of α with radius in the purely magnetic wind case. The results of our exercise are summarized hereafter.

(i) The mass radius and the 95 per cent flux radius have different behaviours in the viscous ($\psi = 0$) and magnetic wind ($\psi = 10^4$) case, expanding in the former and shrinking or plateauing in the latter (when $\alpha \gtrsim 10^{-3}$);

(ii) Current observations cannot discriminate between viscous and magnetic wind models because they are not sensitive enough to recover the potentially faint and viscously expanding outer disc regions. Deeper surveys in star-forming regions with a large age difference could be fruitful to observe the predicted differences between dust disc size evolution in viscous and magnetic wind models. None the less, such observations could be challenging even for ALMA;

(iii) The model predictions are in agreement with the currently available observationally inferred dust disc sizes from Lupus, Chamaeleon I, and Upper Sco Band 7 (0.89 mm) data within 1σ about the median, regardless of ψ. Some purely magnetic wind models predict smaller sizes than in the data. This is not necessarily a problem given the limited angular resolution of the current surveys. None of the models can explain very large discs. A possible explanation is that several of these sources are sub-structured;

(iv) Our models predict smaller flux sizes for longer wavelengths because radial drift segregates the largest grains in the inner disc. This is in contrast with disc sizes inferred from Band 3 (3.10 mm) Lupus observations, which are in line with Band 7 ones;

(v) In Lupus, our models predict a similar size–luminosity correlation as the one detected at 0.89 mm and (marginally) at 3.10 mm. In Upper Sco, however, the slope of the correlation is steeper in the models than in the data.

A more fruitful comparison with the data would be possible by exploring the model dependence on other key parameters, such as the initial disc mass, stellar mass, temperature, and ultimately running disc population synthesis models where the initial conditions are randomly chosen from observationally motivated parameter distributions. Predictions on the size evolution in the presence of sub-structures are also required to interpret the data.

ACKNOWLEDGEMENTS

We thank the anonymous reviewer for their comments that helped to improve the manuscript. FZ acknowledges support from STFC and Cambridge Trust for a PhD studentship. GR acknowledges support from the Netherlands Organisation for Scientific Research (NWO, program number 016.Veni.192.233) and from an STFC Ernest Rutherford Fellowship (grant number ST/T003855/1). This work was supported by the European Union's Horizon 2020 research and innovation programme under the Marie Sklodowska Curie grant agreement number 823823 (DUSTBUSTERS).

Software: NUMPY (Harris et al. 2020), MATPLOTLIB (Hunter 2007), SCIPY (Virtanen et al. 2020), JUPYTERNOTEBOOK (Kluyver et al. 2016), SEABORN (Waskom 2021).

DATA AVAILABILITY

The code used in this paper is publicly available on GitHub at `github.com/rbooth200/DiscEvolution`. The data underlying this paper are available in the ALMA archive as explained in Hendler et al. (2020) and Tazzari et al. (2021a, b). The PPVII chapter summary table of Manara et al. (2022) can be found at `ppvii.org/chapter/15/`.

REFERENCES

Andrews S. M., 2020, ARA&A, 58, 483
Andrews S. M., Terrell M., Tripathi A., Ansdell M., Williams J. P., Wilner D. J., 2018a, ApJ, 865, 157
Andrews S. M. et al., 2018b, ApJ, 869, L41
Ansdell M. et al., 2016, ApJ, 828, 46
Ansdell M. et al., 2018, ApJ, 859, 21
Arakawa S., Matsumoto Y., Honda M., 2021, ApJ, 920, 27
Armitage P. J., Simon J. B., Martin R. G., 2013, ApJ, 778, L14
Bai X.-N., 2013, ApJ, 772, 96
Bai X.-N., 2016, ApJ, 821, 80
Bai X.-N., 2017, ApJ, 845, 75
Bai X.-N., Stone J. M., 2013, ApJ, 769, 76
Balbus S. A., Hawley J. F., 1991, ApJ, 376, 214
Bans A., Königl A., 2012, ApJ, 758, 100
Banzatti A., Pascucci I., Edwards S., Fang M., Gorti U., Flock M., 2019, ApJ, 870, 76
Barenfeld S. A., Carpenter J. M., Ricci L., Isella A., 2016, ApJ, 827, 142
Barenfeld S. A., Carpenter J. M., Sargent A. I., Isella A., Ricci L., 2017, ApJ, 851, 85
Béthune W., Lesur G., Ferreira J., 2017, A&A, 600, A75
Birnstiel T., Andrews S. M., 2014, ApJ, 780, 153
Birnstiel T., Dullemond C. P., Brauer F., 2010, A&A, 513, A79
Birnstiel T., Klahr H., Ercolano B., 2012, A&A, 539, A148
Birnstiel T., Fang M., Johansen A., 2016, Space Sci. Rev., 205, 41
Blandford R. D., Payne D. G., 1982, MNRAS, 199, 883
Bohlin R. C., Savage B. D., Drake J. F., 1978, ApJ, 224, 132
Booth R. A., Clarke C. J., 2021, MNRAS, 502, 1569
Booth R. A., Owen J. E., 2020, MNRAS, 493, 5079
Booth R. A., Clarke C. J., Madhusudhan N., Ilee J. D., 2017, MNRAS, 469, 3994
Booth A. S. et al., 2021, ApJS, 257, 16
Brauer F., Dullemond C. P., Henning T., 2008, A&A, 480, 859
Chiang E. I., Goldreich P., 1997, ApJ, 490, 368
Clarke C. J., Gendrin A., Sotomayor M., 2001, MNRAS, 328, 485
Comerón F., 2008, in Reipurth B., ed, Handbook of Star Forming Regions, Volume II: The Southern Sky, Vol. 5. ASP Monograph Publications, San Francisco, p. 295
de Valon A., Dougados C., Cabrit S., Louvet F., Zapata L. A., Mardones D., 2020, A&A, 634, L12
Dipierro G., Laibe G., Alexander R., Hutchison M., 2018, MNRAS, 479, 4187
Drake J. J., Ercolano B., Flaccomio E., Micela G., 2009, ApJ, 699, L35
Dullemond C. P., Dominik C., 2005, A&A, 434, 971
Ellerbroek L. E. et al., 2014, A&A, 563, A87

Facchini S., Birnstiel T., Bruderer S., van Dishoeck E. F., 2017, A&A, 605, A16
Facchini S. et al., 2019, A&A, 626, L2
Fang M. et al., 2018, ApJ, 868, 28
Fedele D., van den Ancker M. E., Henning T., Jayawardhana R., Oliveira J. M., 2010, A&A, 510, A72
Ferreira J., 1997, A&A, 319, 340
Ferreira J., Pelletier G., 1995, A&A, 295, 807
Flaherty K. M. et al., 2017, ApJ, 843, 150
Flaherty K. M., Hughes A. M., Teague R., Simon J. B., Andrews S. M., Wilner D. J., 2018, ApJ, 856, 117
Flaherty K. et al., 2020, ApJ, 895, 109
Gaia Collaboration, 2021, A&A, 649, A1
Gammie C. F., 1996, ApJ, 457, 355
Gárate M., Birnstiel T., Drążkowska J., Stammler S. M., 2020, A&A, 635, A149
Giacalone S., Teitler S., Königl A., Krijt S., Ciesla F. J., 2019, ApJ, 882, 33
Gressel O., Ramsey J. P., Brinch C., Nelson R. P., Turner N. J., Bruderer S., 2020, ApJ, 896, 126
Gundlach B., Blum J., 2015, ApJ, 798, 34
Harris C. R. et al., 2020, Nature, 585, 357
Harrison R. E. et al., 2021, ApJ, 908, 141
Hartmann L., Herczeg G., Calvet N., 2016, ARA&A, 54, 135
Hendler N., Pascucci I., Pinilla P., Tazzari M., Carpenter J., Malhotra R., Testi L., 2020, ApJ, 895, 126
Hunter J. D., 2007, Comput. Sci. Eng., 9, 90
Kenyon S. J., Hartmann L., 1987, ApJ, 323, 714
Kluyver T. et al., 2016, in Loizides F., Scmidt B., eds, Positioning and Power in Academic Publishing: Players, Agents and Agendas. IOS Press, Amsterdam, p. 87
Koepferl C. M., Ercolano B., Dale J., Teixeira P. S., Ratzka T., Spezzi L., 2013, MNRAS, 428, 3327
Kratter K., Lodato G., 2016, ARA&A, 54, 271
Laibe G., Price D. J., 2014, MNRAS, 444, 1940
Lesur G., 2020, preprint (arXiv:2007.15967)
Lesur G. R. J., 2021, A&A, 650, A35
Lodato G., Scardoni C. E., Manara C. F., Testi L., 2017, MNRAS, 472, 4700
Long F. et al., 2018a, ApJ, 863, 61
Long F. et al., 2018b, ApJ, 869, 17
Long F. et al., 2019, ApJ, 882, 49
Louvet F. et al., 2016, A&A, 596, A88
Louvet F., Dougados C., Cabrit S., Mardones D., Ménard F., Tabone B., Pinte C., Dent W. R. F., 2018, A&A, 618, A120
Luhman K. L. et al., 2008, ApJ, 675, 1375
Lynden-Bell D., Pringle J. E., 1974, MNRAS, 168, 603
Madhusudhan N., 2019, ARA&A, 57, 617
Manara C. F. et al., 2016, A&A, 591, L3
Manara C. F. et al., 2019, A&A, 628, A95
Manara C. F., Ansdell M., Rosotti G. P., Hughes A. M., Armitage P. J., Lodato G., Williams J. P., 2022, preprint (arXiv:2203.09930)
Maret S. et al., 2020, A&A, 635, A15
Mathis J. S., Rumpl W., Nordsieck K. H., 1977, ApJ, 217, 425
Maury A. J. et al., 2019, A&A, 621, A76
Miotello A., Testi L., Lodato G., Ricci L., Rosotti G., Brooks K., Maury A., Natta A., 2014, A&A, 567, A32
Miotello A., Rosotti G., Ansdell M., Facchini S., Manara C. F., Williams J. P., Bruderer S., 2021, A&A, 651, A48
Miotello A., Kamp I., Birnstiel T., Cleeves L. I., Kataoka A., 2022, preprint (arXiv:2203.09818)
Miyake T., Suzuki T. K., Inutsuka S.-I., 2016, ApJ, 821, 3
Morbidelli A., Raymond S. N., 2016, J. Geophys. Res.: Planets, 121, 1962
Najita J. R., Bergin E. A., 2018, ApJ, 864, 168
Öberg K. I., Bergin E. A., 2021, Phys. Rep., 893, 1
Owen J. E., Ercolano B., Clarke C. J., Alexander R. D., 2010, MNRAS, 401, 1415
Pascucci I. et al., 2016, ApJ, 831, 125
Pascucci I. et al., 2020, ApJ, 903, 78
Pinilla P., Birnstiel T., Ricci L., Dullemond C. P., Uribe A. L., Testi L., Natta A., 2012, A&A, 538, A114
Pinilla P., Pascucci I., Marino S., 2020, A&A, 635, A105
Pinilla P., Lenz C. T., Stammler S. M., 2021, A&A, 645, A70
Preibisch T., Brown A. G. A., Bridges T., Guenther E., Zinnecker H., 2002, AJ, 124, 404
Rodenkirch P. J., Dullemond C. P., 2022, A&A, 659, A42
Rosotti G. P., Clarke C. J., Manara C. F., Facchini S., 2017, MNRAS, 468, 1631
Rosotti G. P., Booth R. A., Tazzari M., Clarke C., Lodato G., Testi L., 2019a, MNRAS, 486, L63
Rosotti G. P., Tazzari M., Booth R. A., Testi L., Lodato G., Clarke C., 2019b, MNRAS, 486, 4829
Safronov V. S., 1972, in Evolution of the Protoplanetary Cloud and Formation of the Earth and Planets. Israel Program for Scientific Translations, Keter Publishing House, Jerusalem, p. 212
Salmeron R., Ireland T. R., 2012, Earth Planet. Sci. Lett., 327, 61
Sanchis E. et al., 2021, A&A, 649, A19
Sellek A. D., Booth R. A., Clarke C. J., 2020a, MNRAS, 492, 1279
Sellek A. D., Booth R. A., Clarke C. J., 2020b, MNRAS, 498, 2845
Shakura N. I., Sunyaev R. A., 1973, A&A, 500, 33
Suzuki T. K., Ogihara M., Morbidelli A., Crida A., Guillot T., 2016, A&A, 596, A74
Tabone B. et al., 2017, A&A, 607, L6
Tabone B., Rosotti G. P., Lodato G., Armitage P. J., Cridland A. J., van Dishoeck E. F., 2022a, MNRAS, 512, L74
Tabone B., Rosotti G. P., Cridland A. J., Armitage P. J., Lodato G., 2022b, MNRAS, 512, 2290
Takahashi S. Z., Muto T., 2018, ApJ, 865, 102
Takeuchi T., Lin D. N. C., 2002, ApJ, 581, 1344
Taki T., Kuwabara K., Kobayashi H., Suzuki T. K., 2021, ApJ, 909, 75
Tanaka H., Himeno Y., Ida S., 2005, ApJ, 625, 414
Tazzari M. et al., 2016, A&A, 588, A53
Tazzari M. et al., 2017, A&A, 606, A88
Tazzari M., Clarke C. J., Testi L., Williams J. P., Facchini S., Manara C. F., Natta A., Rosotti G., 2021a, MNRAS, 506, 2804
Tazzari M. et al., 2021b, MNRAS, 506, 5117
Testi L. et al., 2014, in Beuther H., Klessen R. S., Dullemond C. P., Henning T., eds, Protostars and Planets VI. University of Arizona Press, Tucson, p. 339
Tobin J. J. et al., 2020, ApJ, 890, 130
Toci C., Rosotti G., Lodato G., Testi L., Trapman L., 2021, MNRAS, 507, 818
Trapman L., Facchini S., Hogerheijde M. R., van Dishoeck E. F., Bruderer S., 2019, A&A, 629, A79
Trapman L., Rosotti G., Bosman A. D., Hogerheijde M. R., van Dishoeck E. F., 2020, A&A, 640, A5
Trapman L., Tabone B., Rosotti G., Zhang K., 2022, ApJ, 926, 61
Tripathi A., Andrews S. M., Birnstiel T., Wilner D. J., 2017, ApJ, 845, 44
Turner N. J., Fromang S., Gammie C., Klahr H., Lesur G., Wardle M., Bai X. N., 2014, in Beuther H., Klessen R. S., Dullemond C. P., Henning T., eds, Protostars and Planets VI. University of Arizona Press, Tucson, p. 411
van der Marel N. et al., 2018, ApJ, 854, 177
Virtanen P. et al., 2020, Nat. Meth., 17, 261
Vlemmings W. H. T. et al., 2019, A&A, 624, L7
Wang L., Bai X.-N., Goodman J., 2019, ApJ, 874, 90
Wardle M., Koenigl A., 1993, ApJ, 410, 218
Waskom M. L., 2021, J. Open Source Softw., 6, 3021
Weidenschilling S. J., 1977, MNRAS, 180, 57
Whelan E. T., Pascucci I., Gorti U., Edwards S., Alexander R. D., Sterzik M. F., Melo C., 2021, ApJ, 913, 43
Whipple F. L., 1972, in Elvius A., ed., From Plasma to Planet. Wiley, New York, p. 211
Winn J. N., Fabrycky D. C., 2015, ARA&A, 53, 409
Wong Y. H. V., Hirashita H., Li Z.-Y., 2016, PASJ, 68, 67

Youdin A. N., Lithwick Y., 2007, Icarus, 192, 588
Zagaria F., Rosotti G. P., Lodato G., 2021, MNRAS, 504, 2235
Zhu Z. et al., 2019, ApJ, 877, L18
Zormpas A. et al., 2022, A&A, 661, 28

SUPPORTING INFORMATION

Supplementary data are available at *MNRAS* online.

APPENDIX A: CODE CONVERGENCE TEST

APPENDIX B: DEPENDENCE ON THE LEVER ARM PARAMETER

APPENDIX C: FINITE DISPERSAL TIME-SCALE

This paper has been typeset from a TEX/LATEX file prepared by the author.